# The response of the Amazon ecosystem to the photosynthetically active radiation fields: Integrating impacts of biomass burning aerosol and clouds in the NASA GEOS Earth System Model

Huisheng Bian[1,2], Eunjee Lee[3,4], Randal D. Koster[4], Donifan Barahona[4], Mian Chin[2], Peter R. Colarco[2], Anton Darmenov[2], Sarith Mahanama[5,4], Michael Manyin[5,4], Peter Norris[3,4], John Shilling[6], Hongbin Yu[2], and Fanwei Zeng[5,4]

[1]Joint Center for Environmental Technology UMBC, Baltimore, MD, 21250, USA
[2]Laboratory for Atmospheres, NASA Goddard Space Flight Center, Greenbelt, MD, 20771, USA
[3]Goddard Earth Sciences Technology and Research, Universities Space Research Association, Columbia, MD 21046, USA
[4]Global Modeling and Assimilation Office, NASA Goddard Space Flight Center, Greenbelt, MD 20771, USA
[5]Science Systems and Applications, Inc., Lanham, MD 20706, USA
[6]Atmospheric Sciences & Global Change Division, Pacific Northwest National Laboratory, Richland, WA 99352, USA

*Correspondence to*: Huisheng Bian (Huisheng.Bian@nasa.gov)

**Abstract**

The Amazon experiences fires every year, and the resulting biomass burning aerosols, together with cloud particles, influence the penetration of sunlight through the atmosphere, increasing the ratio of diffuse to direct photosynthetically active radiation (PAR) reaching the vegetation canopy and thereby potentially increasing ecosystem productivity. In this study, we use the NASA Goddard Earth Observing System (GEOS) model with coupled aerosol, cloud, radiation, and ecosystem modules to investigate the impact of Amazon biomass burning aerosols on ecosystem productivity, as well as the role of the Amazon's clouds in tempering this impact. The study focuses on a seven-year period (2010-2016) during which the Amazon experienced a variety of dynamic environments (e.g., La Niña, normal years, and El Niño). The direct radiative impact of biomass burning aerosols on ecosystem productivity—called here the aerosol diffuse radiation fertilization effect —is found to increase Amazonian Gross Primary Production (GPP) by 2.6% via a 3.8% increase in diffuse PAR (DFPAR) despite a 5.4% decrease in direct PAR (DRPAR) on multiyear average during burning seasons. On a monthly basis, this increase in GPP can be as large as 9.9% (occurring in August 2010). Consequently, the net primary production (NPP) in Amazon is increased by 1.5%, or ~92 Tg C a$^{-1}$– equivalent to ~37% of the average carbon lost due to Amazon fires over the seven years considered. Clouds, however, strongly regulate the effectiveness of the aerosol diffuse radiation fertilization effect. The efficiency of this fertilization effect is the highest in cloud-free conditions and linearly decreases with increasing cloud amount until the cloud fraction reaches ~0.8, at which point the aerosol-influenced light changes from being a stimulator to an inhibitor of plant growth. Nevertheless, interannual changes in the overall strength of the aerosol diffuse radiation fertilization effect are primarily controlled by the large interannual changes in biomass burning aerosols rather than by changes in cloudiness during the studied period.

## 1. Introduction

The Amazon is home to more than 34 million people and hosts a large variety of plants and animals. The rainforest plays a vital role in the global climate, regulating temperatures and storing vast quantities of carbon (Laurance 1999; Nepstad et al., 2008). It is matter of intense research whether light or water is the limiting factor that controls plant growth over Amazonia. Considerable evidence demonstrates that sunlight indeed drives Amazon forest growth (Doughty et al., 2019; Huete et al., 2006; Myneni et al., 2007) although water deficit could be a limiting factor during severe droughts (Doughty et al., 2015; Feldpausch et al., 2016; Saatchi et al., 2013). Satellite observations show a clear seasonal cycle with a gradual crescendo in both leaf area and incoming surface sunlight beginning at the onset of the dry season (~August – November) (Myneni et al., 2007). Vegetation index maps also show that a majority of Amazonia is greener in the dry season than in the wet season (~mid-December – mid-May) (Huete et al., 2006). It is in the dry season, when more light reaches the canopy level, that the Amazon forest thrives.

Plant photosynthesis requires sunlight to reach the leaves of the canopy. While aerosols and clouds in the atmosphere decrease the total amount of light that reaches the canopy, they also increase scattering, thereby increasing the ratio of diffuse radiation to direct radiation. This is important because the efficiency of plant photosynthesis increases under diffuse sunlight – a phenomenon both explained theoretically (Rap et al., 2015; Roderick et al., 2001; Zhou et al., 2020) and observed in the field (Cirino et al., 2014; Doughty et al., 2010; Ezhova et al., 2018; Gu et al., 2003; Lee et al., 2018; Niyogi et al., 2004; Oliveira et al., 2007). Leaf photosynthesis increases nonlinearly with solar radiation, becoming saturated on bright days at light levels above which leaves cannot take more light (Gu et al., 2003; Mercado et al., 2009). Under clear and clean sky conditions, particularly around midday, sunlight is mainly direct, and while this allows the sunlit leaves on top to be light saturated, the shaded leaves below them receive relatively little sunlight and thus participate less in photosynthesis (Rap et al., 2015; Roderick et al., 2001). In contrast, under cloudy conditions or in the presence of aerosols, much of the midday light is diffuse, and diffuse light can penetrate deeper into the canopy and illuminate shaded leaves. Li and Yang (2015) conducted a chamber experiment to explore diffuse light on light distribution within a canopy and the resulting effects on crop photosynthesis and plant growth. They concluded that diffusion of the incident light improves spatial light distribution, lessens the variation of temporal light distribution in the canopy, and allows more light-stimulated growth of shade-tolerant potted plants.

The situation is more profound during the Amazon dry season when intensive seasonal fires release large amounts of primary aerosol particles as well as gas precursors that form secondary organic and inorganic aerosols. Using stand-alone radiation and vegetation models, Rap et al. (2015) concluded that fires over the Amazon dry season increase Amazon net primary production (NPP) by 1.4–2.8% by increasing diffuse radiation. This enhancement of Amazon basin NPP (78–156 Tg C $a^{-1}$) is equivalent to 33–65% of the annual regional carbon emissions from biomass burning and accounts for 8–16% of the observed carbon sink across mature Amazonian forests. Moreira et al. (2017) advanced this analysis by coupling an ecosystem module and aerosol model within a Eulerian transport model. Their study indicated that biomass burning aerosols lead to increases of about 27% in Amazonian Gross Primary Production (GPP) and 10% in plant respiration as well as a decline in soil respiration of 3%. However, their

93    approach assumes cloud-free conditions through their use of a diffuse irradiance
94    parameterization based on the multiwavelength aerosol optical depth (AOD) measurement.
95    Malavelle et al. (2019) explored the overall net impact of biomass burning aerosol on the
96    Amazon ecosystem using an Earth System Model (ESM) (HadGEM2-ES). They estimated NPP
97    to increase by +80 to +105 Tg C $a^{-1}$, or 1.9% to 2.7%, ascribing this net change to an increase in
98    diffuse light, a reduction in the total amount of radiation, and feedback from climate adjustments
99    in response to the aerosol forcing. Their study takes into account the dynamic feedback of short
100   lifetime cloud fields. However, the authors have not explicitly quantified the impact of Amazon
101   background clouds and their interannual changes in tempering the aerosol diffuse radiation
102   fertilization effect (DRFE).

104   When clouds and aerosol co-exist, the impact from clouds on the ecosystem typically dominates
105   because clouds are optically thicker. The surface sunlight for cloudy versus cloud-free conditions
106   can differ greatly even if the AOD is the same. (Note that, unless specified otherwise, solar
107   radiation in this study refers to the wavelength range of 400-700 nm, i.e., photosynthetically
108   active radiation, or PAR). Measurements indicate that the desirable range of clearness index (CI)
109   -- the ratio of total (i.e., direct plus diffuse) light at surface to the total incoming light at top of
110   atmosphere -- is around 0.4-0.7 for some forest ecosystems and above 0.3 for peatland (Butt et
111   al., 2010, Letts and Lafleur, 2005). Quite often a low CI occurs during a cloudy day, but on
112   occasion it might result from the presence of a very thick aerosol layer. As suggested above, if
113   CI is high, the diffuse fraction of the total solar radiation is low, and the overall productivity of
114   the canopy is reduced. For example, Cirino et al. (2014) found that the net ecosystem exchange
115   (NEE) of $CO_2$ is increased by 29% and 20% in two Amazon stations, the Jaru Biological Reserve
116   (RBJ) and the Cuieiras Biological Reserve at the K34 Large-Scale Biosphere-Atmosphere
117   Experiment in Amazonia (LBA) tower, respectively, when AOD is 0.1-1.5 at 550nm under clear
118   conditions. Higher AOD (> 3) leads to a strong reduction in photosynthesis (via reducing PAR)
119   up to the point where NEE approaches zero. Oliveira et al. (2007) found that Amazon forest
120   productivity was enhanced under moderately thick smoke loading because of an increase of
121   diffuse solar radiation, but large aerosol loading (i.e., AOD > 2.7) results in lower net
122   productivity of the Amazon forest.

124   Despite its name, the Amazon's "dry season" (June-November) still features significant
125   cloudiness, and the interannual variations in the clouds can be large. Furthermore, rain does fall
126   during the dry season – close to 40% of the total annual precipitation falls therein (Li et al.,
127   2006). Clouds in the dry season are mostly formed by small-scale processes that influence the
128   weather (see an example of a uniform layer of "popcorn" clouds observed by Moderate
129   Resolution Imaging Spectroradiometer (MODIS) on 08/19/2009 in
130   http://earthobservatory.nasa.gov/IOTD/view.php?id=39936). It is during this period, when
131   sunlight (particularly diffuse light) shines on the trees due to reduced rain (and fewer clouds)
132   relative to the wet season, that the forest grows the most. Consideration of the joint effects of
133   clouds and biomass burning aerosols on diffuse and direct PAR during the dry season is thus
134   particularly important.

136   This study has two objectives. First, we investigate how Amazon biomass burning aerosols
137   (BBaer) affect the land productivity (i.e., GPP and NPP) via their impact on direct and diffuse
138   PAR (DRPAR and DFPAR). Second, we investigate the sensitivity of the BBaer DRFE to the

139  presence of the Amazon dry season cloud fields within the range indicated by the interannual
140  variation of the clouds. We use in our analysis a version of the NASA GEOS ESM that includes
141  coupling between aerosol, cloud, radiation, and ecosystem processes. To our knowledge, only
142  one other study has used an ESM to investigate such fire impacts across Amazonia (Malavelle et
143  al., 2019), and as noted above, that study did not address the ability of Amazon clouds to temper
144  the BBaer impacts. Accordingly, our study is the first ESM-based study to investigate the BBaer
145  DRFE within a range of interannual Amazon cloud levels. Together our objectives provide a full
146  and comprehensive study of BBaer DRFE in a context of potential Amazon dry season
147  atmospheric conditions.
148
149  It is necessary to point out, however, that our study focuses only on the impact of Amazon
150  biomass burning aerosol. We do not consider the radiative impacts of other potentially important
151  aerosols. These other aerosol types have been examined in various observational studies (e.g.,
152  Cirino et al., 2014; Ezhova et al., 2018; Hemes et al., 2020; Wang et al., 2018, Yan et al., 2014)
153  and model investigations that focus, for example, on anthropogenic aerosol (Keppel et al., 2016);
154  O'Sullivan et al., 2016), dust (Xi et al., 2012), biogenic aerosol (Rap et al., 2018; Sporre et al.,
155  2019), volcanic aerosol (Gu et al., 2003), and the general aerosol field (Feng et al., 2019).
156
157  The paper is organized as follows. Section 2 describes the NASA GEOS ESM and its relevant
158  modules (section 2.1), the observational data used for model evaluation and explanation (section
159  2.2), and the experimental setup (section 2.3). Section 3 provides an evaluation of the model
160  (section 3.1), basic theory regarding the impact of aerosol and cloud on the surface downward
161  radiation (section 3.2), results regarding the simulated ecosystem response to BBaer-induced
162  radiation changes (section 3.3), and the impacts of Amazon background clouds on this response
163  (section 3.4). A final summary is provided in section 4.
164
165  **2. Model description, data application, and experiment setup**
166
167  **2.1 Model description**
168  The GEOS modeling system connects state-of-the-art models of the various components of the
169  Earth's climate system together using the Earth System Modeling Framework (ESMF) (Molod et
170  al., 2015; 2012; Rienecker et al., 2011; https://gmao.gsfc.nasa.gov/). We discuss here the
171  components of the system that are particularly relevant to our study, including aerosol, cloud
172  microphysics, radiative transfer, and land ecosystem modules.
173
174  GEOS Goddard Chemistry Aerosol Radiation and Transport (GOCART) simulates a number of
175  major atmospheric aerosol species and precursor gases from natural and anthropogenic sources,
176  including sulfate, nitrate, ammonium, black carbon (BC), organic aerosol (OA, including
177  primary and secondary OA), dust, sea salt, dimethyl sulfide (DMS), $SO_2$, and $NH_3$ (Bian et al.,
178  2010, 2013, 2017, 2019; Chin et al., 2009, 2014; Colarco et al., 2010, 2017; Murphy et al., 2019;
179  Randles et al., 2013). Monthly emissions from shipping, aircraft, and other anthropogenic
180  sources are obtained from the recent Coupled Model Intercomparison Project version 6
181  (CMIP6) Community Emissions Data System (CEDS). Daily biomass burning emissions are
182  provided by Global Fire Emissions Database (GFED4s)
183  (https://daac.ornl.gov/VEGETATION/guides/fire_emissions_v4.html). Estimates of degassing
184  and eruptive volcanic emissions are derived from Ozone Monitoring Instrument (OMI) satellite

185    (Carn et al., 2017). Emissions of dust, sea salt, and DMS are dynamically calculated online as a
186    function of the model-simulated near-surface winds and other surface properties. A more recent
187    development of GOCART relevant to this study involves the modification of the absorbing
188    properties of "brown carbon" from biomass burning organic aerosols (Colarco et al., 2017) and
189    the inclusion of secondary organic aerosol (SOA) produced via chemical reactions of volatile
190    organic compounds (VOCs) emitted from anthropogenic and biomass burning sources, following
191    the approach developed by Hodzic and Jimenez (2011) and Kim et al. (2015). In addition, the
192    SOA from biogenic sources has been updated with its precursor gases of isoprene and
193    monoterpene emissions calculated online as a function of light and temperature using the Model
194    of Emissions of Gases and Aerosols from Nature (MEGAN) version 2.1 (Guenther et al., 2012),
195    assuming SOA yield of 3% from isoprene and 5% from monoterpene oxidations (Kim et al.,
196    2015).
197
198    The GEOS two-moment cloud microphysics module is used in this study. The module includes
199    the implementation of a comprehensive stratiform microphysics module, a new cloud coverage
200    scheme that allows ice supersaturation, and a new microphysics module embedded within the
201    moist convection parameterization (Barahona et al., 2014). At present, aerosol number
202    concentrations are derived from the GEOS/GOCART-calculated aerosol mass mixing ratio and
203    prescribed size distributions and mixing state, which are then used for cloud condensation nuclei
204    (CCN) activation (following the approach of Abdul-Razzak and Ghan, 2000) and ice nucleation
205    (following the approach of Barahona and Nenes, 2009) processes. Aerosol-cloud interactions are
206    thus accounted for in our simulation. The model calculates various cloud properties, including
207    cloud fraction, cloud droplet and ice crystal number concentrations and effective radii, and cloud
208    liquid and ice water paths. These fields have been evaluated against satellite observations and
209    field measurements; the model shows a realistic simulation of cloud characteristics despite a few
210    remaining deficiencies (Barahona et al., 2014, Breen et al., 2020).
211
212    The current default GEOS solar radiation transfer module is the shortwave rapid radiation
213    transfer model for general circulation models (RRTMG_SW), a correlated k-distribution model
214    (Iacono et al., 2008). This General Circulation Model (GCM) version utilizes a reduced
215    complement of 112 g-points, which is half of the 224 g-points used in the standard
216    RRTMG_SW, and a two-stream method for radiative transfer. Total fluxes are accurate to within
217    1-2 W m$^{-2}$ relative to the standard RRTMG_SW (using Discrete Ordinates Radiative Transfer,
218    DISORT) with aerosols in clear sky and within 6 W m$^{-2}$ in overcast sky.  RRTMG_SW with
219    DISORT is itself accurate to within 2 W m$^{-2}$ of the data-validated multiple scattering model,
220    CHARTS. RRTMG_SW specifically calculates the direct and diffuse components of PAR (400-
221    700 nm) separately. The GEOS atmospheric radiative transfer calculation is designed in a way
222    that allows users to examine the impact of various combinations of atmospheric aerosol and
223    cloud fields on radiation. In addition to the standard calculation of solar radiation for ambient
224    atmospheric conditions, diagnostic calculations can be carried out by repeating the calculation of
225    the radiation transfer scheme with different combinations of atmospheric conditions: clean air
226    (no aerosols), clear air (no clouds), and clean plus clear air. Using this architecture, for this study
227    we modify the radiation scheme to allow the additional diagnosis of radiation fields under
228    conditions of zero BBaer but retained non-BBaer and ambient clouds.
229

230 The catchment land surface model (LSM) with carbon and nitrogen physics (Catchment-CN) in
231 GEOS is in essence a merger of the C-N physics within the NCAR–DOE Community Land
232 Model (CLM) (Oleson et al. 2010, 2013; Lawrence et al., 2019) version 4.0 and the energy and
233 water balance calculations of the NASA GMAO catchment LSM (Koster et al. 2000). The
234 original NASA catchment LSM used a prescribed representation of phenology (leaf area index,
235 or LAI, and greenness fraction) to compute the canopy conductance, the parameter describing
236 the ease with which the plants transpire water. The light interception by vegetation in the GEOS
237 Catchment-CN utilizes the same parameterization as that in CLM4. The photosynthesis and
238 transpiration depend non-linearly on solar radiation. The canopy is assumed to consist of sunlit
239 leaves and shaded leaves, and the DRPAR and DFPAR absorbed by the vegetation is
240 apportioned to the sunlit and shaded leaves as described by Thornton and Zimmermann (2007).
241 The prognostic carbon storages underlying the phenological variables are computed as a matter
242 of course along with values of canopy conductance that reflect an explicit treatment of
243 photosynthesis physics. These canopy conductances, along with the LAIs diagnosed from the
244 new carbon prognostic variables, are fed into the energy and water balance calculations in the
245 original catchment LSM. The output fluxes from the merged system include carbon fluxes in
246 addition to traditional fluxes of heat and moisture. The merger of the two models allows
247 Catchment-CN to follow 19 distinct vegetation types. Koster and Walker (2015) have used
248 Catchment-CN within an atmospheric global circulation model (AGCM) framework to
249 investigate interactive feedback among vegetation phenology, soil moisture, and temperature. In
250 this study, the modeled atmospheric $CO_2$ from the AGCM is used to drive the carbon, water, and
251 energy dynamics in the Catchment-CN model.

252 In addition to the GEOS ESM, we use a photolysis scheme, FastJX, in its stand-alone mode to
253 explore how incoming solar radiation penetrates the atmosphere in the presence of aerosols and
254 clouds in order to enhance our basic understanding of the role of atmospheric particles on
255 radiation. FastJX is based on the original Fast-J scheme, which was developed for tropospheric
256 photochemistry with interactive consideration of aerosol and cloud impacts at 291–850 nm (Wild
257 et al., 2000), and Fast-J2, which extended the scheme into the deep UV spectrum range of 177-
258 291 nm (Bian and Prather, 2002).
259
260 **2.2 Observational data**
261 We mostly rely on the GoAmazon ("Green Ocean Amazon") field campaign
262 (http://campaign.arm.gov/goamazon2014/) for in situ aerosol observations to assess the model-
263 simulated OA concentrations. GoAmazon is an integrated field campaign conducted in the
264 central Amazon Basin (Martin et al., 2016). Specifically, the following datasets are used: (a) the
265 surface OA concentration measured in 2014 by the Aerosol Chemical Speciation Monitor
266 (ACSM) operated by the Department of Energy's (DOE) Atmospheric Radiation Measurement
267 (ARM) Mobile Facility located 70 km downwind of Manaus, Brazil (Ng et al., 2011), (b) the
268 surface CO volume mixing ratio in 2014 at Manaus measured by Los Gatos Research (LGR)
269 $N_2O$/CO Analyzer that uses LGR's patented Off-axis Integrated Cavity Output Spectroscopy
270 (ICOS) technology, and (c) the vertical profile of OA concentration measured by a time-of-Flight
271 Aerosol Mass Spectrometer (ToF-AMS) instrument on the ARM Aerial Facility Gulfstream-1
272 (G-1) aircraft during the dry season of 2014 (Sept 06-Oct 04, 2014) (Shilling et al., 2018). The
273 G-1 aircraft was based out of the Manaus International airport and flew patterns designed to
274 intersect the Manaus urban plume at increasing downwind distance from the city (e.g., 59-61° W
275 and 4-2.5° S). In addition, we evaluate the model with AOD and single scattering albedo (SSA)

276 measurements taken at a central Amazon station (Alta Floresta) in the ground-based Aerosol
277 Robotic Network (AERONET) sun photometer network (http://aeronet.gsfc.nasa.gov). We also
278 use MODIS collection 6.1 level-3 AOD product
279 (http://modis.gsfc.nasa.gov/data/dataprod/index.php), which is characterized by observations
280 with large spatial coverage.
281
282 MODIS cloud products (https://modis-atmosphere.gsfc.nasa.gov/data/dataprod/), specifically
283 total cloud fraction and cloud optical depth in liquid and ice particles, are used to evaluate the
284 model cloud simulation. We use the cloud data from MODIS collection 6.1 MYD08_D3, a level-
285 3 1°×1° global gridded monthly joint product derived from the MODIS level 2 pixel level
286 products. MODIS level 2 cloud fraction is produced by the infrared retrieval methods during
287 both day and night at a 5×5 1-km-pixel resolution. Level 2 cloud optical thickness used in this
288 study is derived using the MODIS visible and near-infrared channel radiances from the Aqua
289 platform.
290
291 The satellite-derived Clouds and the Earth's Radiant Energy System product CERES-EBAF is
292 used to evaluate the GEOS simulation of radiation fields. CERES-EBAF retrieves surface
293 downward shortwave radiation ($R_{SFC}$) using cloud information from more recent satellite data
294 (MODIS, CERES, CloudSat and CALIPSO) and aerosol fields from AERONET/MODIS
295 validation-based estimates (Kato et al., 2013). This global product is provided at a 1°×1°
296 horizontal resolution and covers the years 2000-2015 for both all- and clear-sky conditions. The
297 multiyear $R_{SFC}$ products provide both a spatial and temporal view of radiation over Amazonia.

298 Two observation-based GPP products (FluxCom and FluxSat) are used to evaluate ecosystem
299 productivity in the GEOS simulations. The FluxCom GPP product provides globally distributed
300 eddy-covariance-based estimates of carbon fluxes between the biosphere and the atmosphere
301 through upscaling using machine learning methods (Jung et al., 2020). FluxSat GPP is estimated
302 with models that use satellite data (e.g., MODIS reflectances and solar-induced fluorescence
303 (SIF)) within a simplified light-use efficiency framework (Joiner et al., 2018). We use monthly
304 GPP of 2010-2015 in this study.

305 **2.3 Experiment setup**
306 All experiments were run with the coupled atmosphere and land components of the NASA
307 GEOS ESM system discussed above. The sea surface temperature (SST) for the atmospheric
308 dynamic circulation is provided by the GEOS Atmospheric Data Assimilation System (ADAS)
309 that incorporates satellite and in situ SST observations and assimilates Advanced Very High
310 Resolution Radiometer (AVHRR) brightness temperatures. The experiments were run in replay
311 mode, which means that the model dynamical variables (winds, pressure, temperature, and
312 humidity) were set, every 6 hours, to the values archived by the Modern-Era Retrospective
313 Analysis for Research and Applications version 2 (MERRA-2) meteorological reanalysis (Gelaro
314 et al. 2017); a 6-hourly forecast provided the dynamical and physical fields between the 6-hour
315 resets. In effect, the replay approach forces the atmospheric "weather" simulated in the model to
316 agree with the reanalysis. This nudging of the GEOS dynamic fields toward the MERRA2
317 reanalysis ensures that the atmospheric conditions of our four simulations (see below) remain
318 close to each other, allowing a more focused study of radiative impact on ecosystem. All
319 designed experiments were run over 2010-2016, a period that includes La Niña (2010-2011), El

320 Niño (2015-2016), and neutral years as indicated by the Oceanic Niño Index (ONI,
321 https://origin.cpc.ncep.noaa.gov/) (Figure S1). Information regarding long-term BB OA
322 emissions (i.e., 1997-2016) and long-term MERRA2 cloud fraction anomalies (i.e., 1995-2018)
323 is shown in Figure S2. The selected period of 2010-2016 represents well the long-term period in
324 terms of the variation of BB emissions and cloud coverage.
325
326 Our experimental design makes extensive use of GEOS's highly flexible configuration. First, the
327 GEOS GOCART module includes a tagged aerosol mechanism. Each specific aerosol
328 component in GOCART is simulated independently from the others, and the contribution of each
329 emission type to the total aerosol mass is also not interfered by that of other emission types.
330 Thus, additional aerosol tracers can easily be "tagged" according to emission source types. This
331 makes it possible for GOCART to calculate and transfer two sets of aerosol fields (e.g., one with
332 and one without a biomass burning source) to the radiation module. Second, the radiation module
333 can in turn calculate a set of atmospheric radiation fields corresponding to each set of aerosol
334 fields, and it can then disseminate both sets of radiation fields to the various components of
335 interest (i.e., cloud module, land ecosystem module, etc.) according to the needs of our
336 experiments (see below).
337
338 Table 1 provides a brief summary of the experiments performed for this study. First, we designed
339 a pair of experiments (allaer and nobbaer, hereafter referred to as "pair1") to explore the BBaer
340 DRFE on the land productivity via PAR (objective 1). The allaer and nobbaer experiments are
341 designed to simulate the same atmospheric dynamics but send different PAR fluxes into the
342 Catchment-CN model. Specifically, both the allaer and nobbaer experiments used all
343 atmospheric aerosols including real-time biomass burning emissions over 2010-2016 to calculate
344 a set of radiation fields ($R^1$) to drive atmospheric circulation; however, with the help of GEOS's
345 flexible configuration, the nobbaer experiment also calculated a second set of radiation fields
346 ($R^2$) that used non-BB aerosols only. $R^1$ was sent to Catchment-CN in the allaer experiment
347 whereas $R^2$ was sent to Catchment_CN in the nobbaer experiment. In this way, the only
348 difference between the allaer and nobbaer experiments was the PAR fluxes used to drive the
349 ecosystem model – only the PAR fluxes used in allaer reflected the presence of biomass burning
350 aerosols. The atmospheric meteorological fields in the two experiments, including clouds, skin
351 temperature, and soil moisture, show only minor differences stemming from land feedback
352 (Figure S3-4, Table 3, Table S1e and Table S2e). A negligible impact on cloud fields has also
353 been reported in Pedruzo-Bagazgoitia et al. (2017).
354
355 Table 1. Designed experiments (2010-2016) with their perturbation on aerosol fields and
356 subsequent impact on radiation and ecosystem

| Exp Name | | Aerosol | R in RRTMG | R driving Atmosphere | R driving Catchment-CN | Purpose |
|---|---|---|---|---|---|---|
| Pair 1 | allaer | Standard all, w/ Realtime AERbb emission | $R^1_{top}$, $R^1_{dir}$, $R^1_{diff}$ (all aerosol) | $R^1_{top}$, $R^1_{dir}$, $R^1_{diff}$ | $R^1_{dir}$, $R^1_{diff}$ | Check atmospheric BB aerosol impact on plants via radiation fields during 2010-2016 |
| | nobbaer | | $R^1_{top}$, $R^1_{dir}$, $R^1_{diff}$ (all aerosol) $R^2_{top}$, $R^2_{dir}$, $R^2_{diff}$ (all non-bb aerosol) | $R^1_{top}$, $R^1_{dir}$, $R^1_{diff}$ | $R^2_{dir}$, $R^2_{diff}$ | |
| Pair 2 | callaer | Standard all, w/ AERbb emission fixed at 2010 | $R^1_{top}$, $R^1_{dir}$, $R^1_{diff}$ (all aerosol) | $R^1_{top}$, $R^1_{dir}$, $R^1_{diff}$ | $R^1_{dir}$, $R^1_{diff}$ | Check how clouds adjust the above impact |
| | cnobbaer | | $R^1_{top}$, $R^1_{dir}$, $R^1_{diff}$ (all aerosol) $R^2_{top}$, $R^2_{dir}$, $R^2_{diff}$ (all non-bb aerosol) | $R^1_{top}$, $R^1_{dir}$, $R^1_{diff}$ | $R^2_{dir}$, $R^2_{diff}$ | |

357

358
359  We also designed a pair of experiments (callaer and cnobbaer, hereafter referred to as "pair2") to
360  address the sensitivity of the BBaer DRFE to the presence of the Amazon dry season cloud fields
361  (objective 2). The pair2 experiments are similar to those in pair1 except that the particular BB
362  emissions of year 2010 were repeated during all seven years. Applying a fixed aerosol emission
363  allows us to attribute the interannual variation of the ecosystem solely to the influence of
364  interannual variations in atmospheric meteorological fields, including clouds. In addition,
365  combining the pair1 and pair2 experiments provides two biomass burning aerosol emissions for
366  each year except 2010, which allows us to compare the impacts of different emissions under
367  similar meteorological environments (Figure S3-4, Table 3, Table S1e and Table S2e). Please
368  note that the experiments in this study were intentionally designed to allow the aerosols to affect
369  the vegetation only through their impact on the direct and diffuse radiation that enters ecosystem
370  and not, for example, through their other potential impacts on the environment. Future study may
371  focus on these other impacts. Given that the experiment period covers strong La Niña and El
372  Niño years, we can examine BBaer impacts on ecosystem productivity under the full range of
373  Amazon background cloud fields.
374
375  ## 3. Results and discussions
376
377  ### 3.1 Evaluation of GEOS simulations of aerosol, cloud, radiation, and ecosystem
378  response
379  The NASA GEOS ESM model, including its aerosol, cloud, radiation, and ecosystem modules as
380  used in the baseline simulation (i.e., experiment allaer), has been evaluated extensively and
381  utilized in a number of scientific studies. However, very few of the past studies with GEOS was
382  concentrated on detailed model evaluation over South America. We provide such an evaluation
383  here.
384
385  The simulated tracer fields are compared with measurements over the Amazon in Figs. 1 and 2.
386  Figure 1 shows results for surface OA concentration, surface CO concentration, and the OA
387  concentration vertical profile. We focus primarily on the OA evaluation since it is the major
388  component of biomass burning aerosols. Figure 1a shows the comparison of surface daily OA
389  concentration between the model simulation and the GoAmazon measurements at Manaus,
390  Brazil, in 2014 (The location is indicated in Fig. 2c with an open-diamond). The simulated OA
391  broadly captures the seasonal trend in OA concentrations measured at Manaus, but it is lower
392  than observed OA values by ~24% during Sept-Oct and ~ 30% annually. For the period of
393  interest, the model simulates a large fire signal in August that is not seen in the measurements.
394  However, this strong August biomass burning signal does show up in the CO measurements (Fig.
395  1b), which should also be from biomass burning. The reasons for such discrepancy from
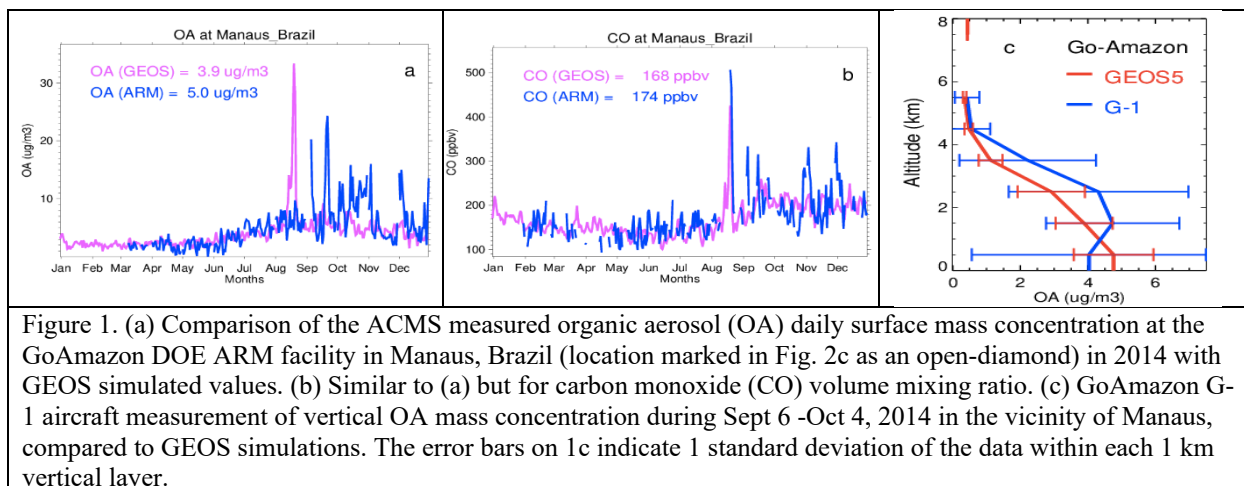396  observations are not clear.
397

Figure 1. (a) Comparison of the ACMS measured organic aerosol (OA) daily surface mass concentration at the GoAmazon DOE ARM facility in Manaus, Brazil (location marked in Fig. 2c as an open-diamond) in 2014 with GEOS simulated values. (b) Similar to (a) but for carbon monoxide (CO) volume mixing ratio. (c) GoAmazon G-1 aircraft measurement of vertical OA mass concentration during Sept 6 -Oct 4, 2014 in the vicinity of Manaus, compared to GEOS simulations. The error bars on 1c indicate 1 standard deviation of the data within each 1 km vertical layer.
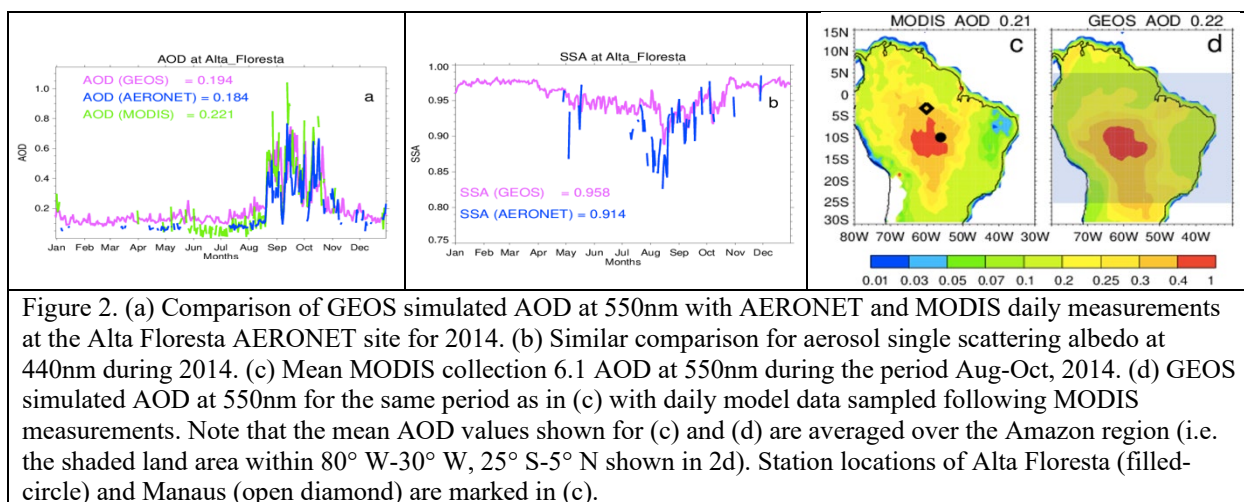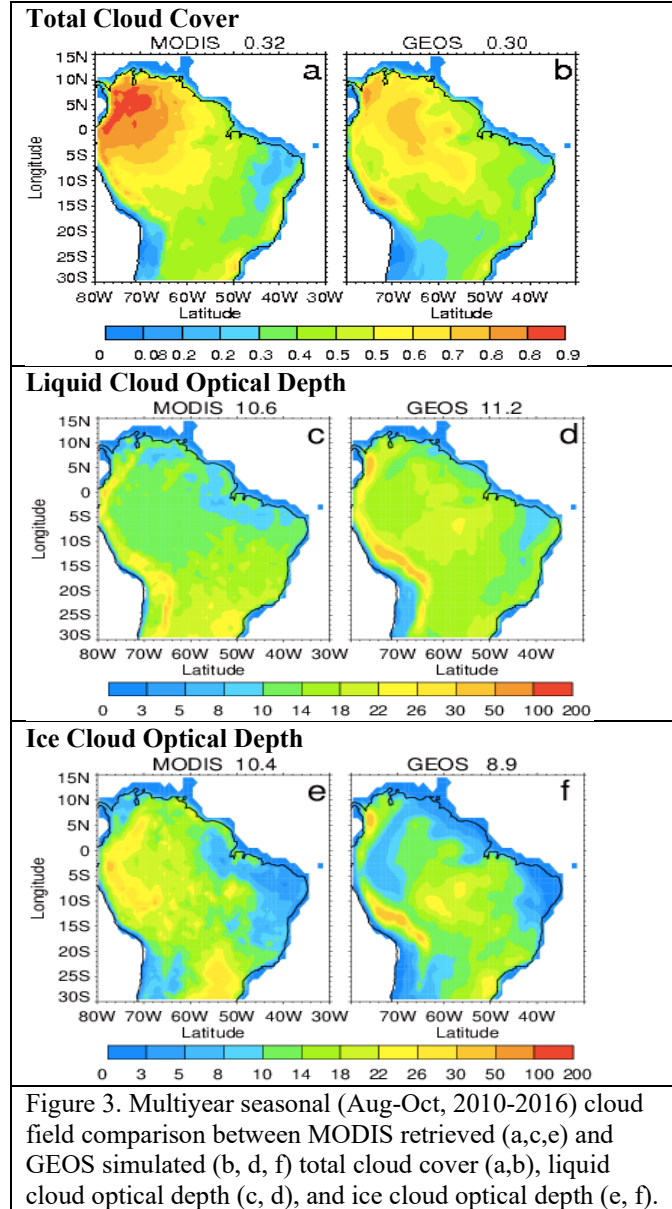
398



Figure 2. (a) Comparison of GEOS simulated AOD at 550nm with AERONET and MODIS daily measurements at the Alta Floresta AERONET site for 2014. (b) Similar comparison for aerosol single scattering albedo at 440nm during 2014. (c) Mean MODIS collection 6.1 AOD at 550nm during the period Aug-Oct, 2014. (d) GEOS simulated AOD at 550nm for the same period as in (c) with daily model data sampled following MODIS measurements. Note that the mean AOD values shown for (c) and (d) are averaged over the Amazon region (i.e. the shaded land area within 80° W-30° W, 25° S-5° N shown in 2d). Station locations of Alta Floresta (filled-circle) and Manaus (open diamond) are marked in (c).

399
400  When compared with aircraft G-1 measurements over a ~2°×2° region around the center of
401  Manaus during the biomass burning season (Sept. 6 – Oct. 4, 2014) (Fig. 1c), the simulated
402  vertical OA concentrations underestimate the measurements above 1 km altitude but
403  overestimate them under it, although they overlap within their standard deviations for all
404  altitudes. Here the model data have been sampled spatially and temporally along the G-1 flight
405  paths. This surface OA overestimation by the model seems to contradict the model's
406  underestimation seen in Fig. 1a, indicating that capturing aerosols at the right times and locations
407  is a challenge.
408
409  Figure 2 shows the AOD (550nm) and SSA (440nm) comparison at the AERONET station of
410  Alta Floresta, which is located close to the area of the most intensive Amazon fires (location is
411  marked in Fig. 2c as a filled-in circle). The model-simulated, AERONET-measured, and
412  MODIS-retrieved AODs at this site agree within 20% (Fig. 2a), all showing a peak of AOD
413  during the biomass burning season. SSA during the burning season generally ranges between
414  0.85 – 0.95 (Fig. 2b). The model agrees with the measurements with accurate better than 5%
415  except during the first half of August, when the model aerosols are too scattering. However, it is
416  puzzling to observe the extremely low measured SSA in the beginning of August given that the
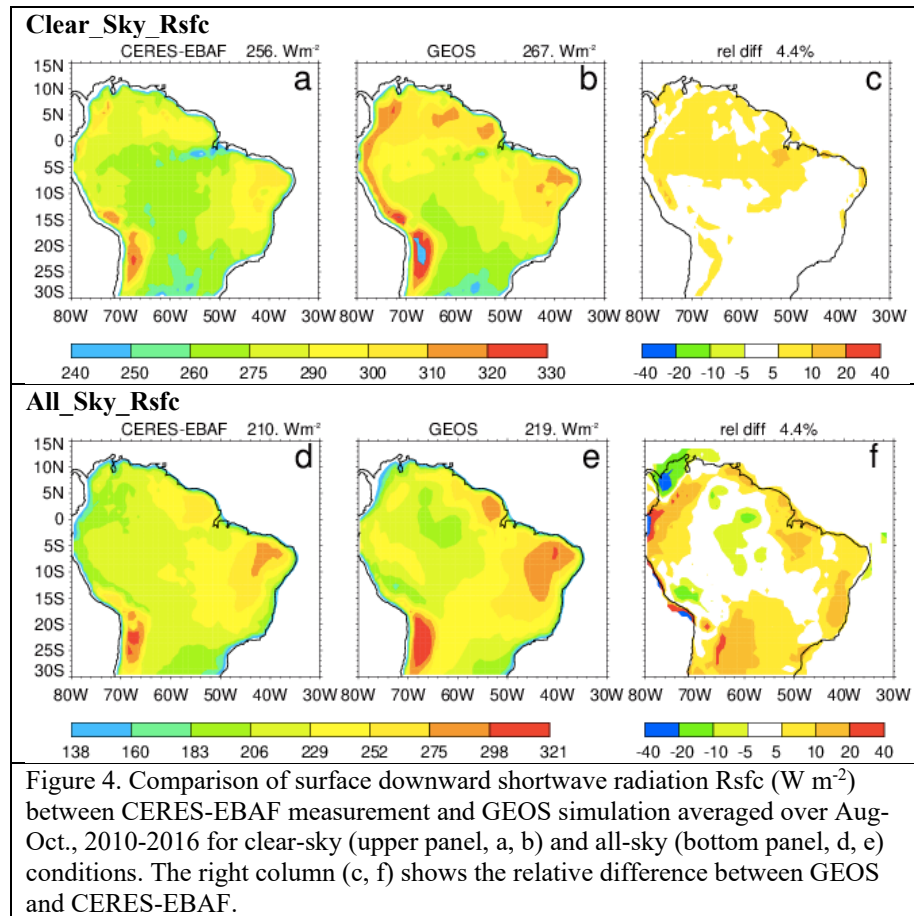417  AOD is still low then, as shown in Fig. 2a. It could be the quality of AERONET SSA is not

418    "reliable" at low AOD (Chin et al., 2009). Because of the low sensitivity to the absorption when
419    aerosol loading is low, SSA is retrieved with sufficiently high accuracy only when the
420    total AOD at 440 nm is equal or higher than 0.4 and solar zenith angle is 50 degree or higher
421    (Dubovik et al., 2000, 2002). Regionally over the Amazon region, defined throughout the study
422    as the land area within 80° W-30° W, 25° S-5° N (shaded land area in Fig. 2d), the model-
423    simulated AOD (0.22 in Fig. 2d) during the biomass burning season generally agrees with
424    MODIS satellite retrievals (0.21 in Fig. 2c). A simulated high bias is seen over the East Amazon;
425    however, though this region is in our area of interest, the bias should have only a minor impact
426    on our study given that the area is relatively bare, with little vegetation coverage.



Figure 3. Multiyear seasonal (Aug-Oct, 2010-2016) cloud
field comparison between MODIS retrieved (a,c,e) and
GEOS simulated (b, d, f) total cloud cover (a,b), liquid
cloud optical depth (c, d), and ice cloud optical depth (e, f).

462    The accurate simulation of cloud fields is also important for our study. In Fig. 3 we evaluate the
463    GEOS-simulated cloud cover fraction and cloud optical depth with MODIS satellite products.

464 Here the GEOS data have been sampled with MODIS overpass time and location. GEOS
465 generally captures the magnitude and main features of the cloud fields observed in MODIS,
466 though with some differences; the model overestimates the cloud quantities over the central
467 Amazon and underestimates them in Northwest South America. The overall difference over the
468 Amazon region between simulated and MODIS-based estimates is less than 7% for cloud cover
469 fraction, 10% for liquid water cloud optical depth, and 15% for ice cloud optical depth. The
470 seasonality of these cloud quantities is shown in Fig. S5a-c to further evaluate the model
471 performance. The model has a better cloud simulation during the period of Aug-Oct, which is the
472 focus period of this study since Amazon fires occur periodically every year in this season.
473
474 Figure 4 shows a comparison between the simulated downward shortwave radiation at the
475 surface and CERES-EBAF measurements averaged over Aug-Oct., 2010-2016 for both clear-sky
476 and all-sky conditions. The comparison of the time series of monthly mean shortwave radiation
477 during 2010-2016 over the Amazon region is shown in Fig. S6. GEOS captures the observed
478 spatial patterns with ~4% high bias for both clear and all sky conditions over the Amazon region.
479



Figure 4. Comparison of surface downward shortwave radiation Rsfc (W m$^{-2}$) between CERES-EBAF measurement and GEOS simulation averaged over Aug-Oct., 2010-2016 for clear-sky (upper panel, a, b) and all-sky (bottom panel, d, e) conditions. The right column (c, f) shows the relative difference between GEOS and CERES-EBAF.

480
481 Following the evaluation approach in Malavelle et al. (2019), we evaluate our model's ability to
482 simulate GPP on the global scale against FluxCom and FluxSat. As mentioned in section 2.2,
483 FluxCom GPP is derived from surface measurements of carbon fluxes whereas FluxSat GPP is
484 derived from satellite data. The comparison of global distribution of multiyear average GPP (Fig.
485 5) and zonal mean multiyear average GPP (Fig. 6) show that GEOS captures the GPP global

distribution seen in the observations, with a GPP peak in tropics. The model does show a second peak in middle latitudes of the Southern Hemisphere but misses the observed peak in the Northern Hemisphere subtropics.
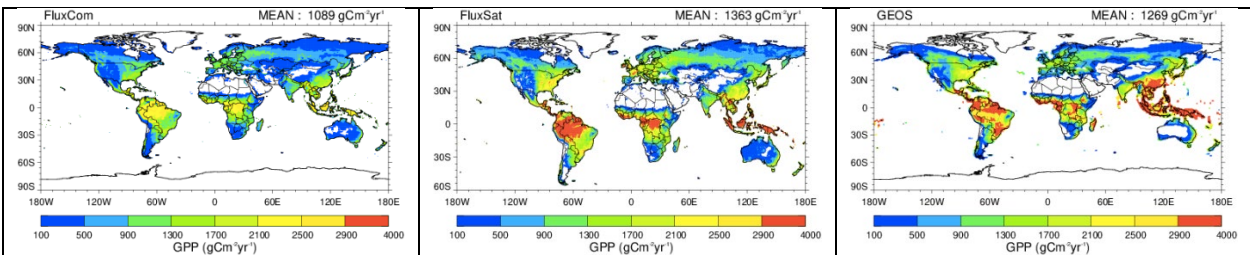


Figure 5. 2010-2015 multiyear average global GPP from FluxCom, FluxSat, and GEOS. The global average value is shown in the top.
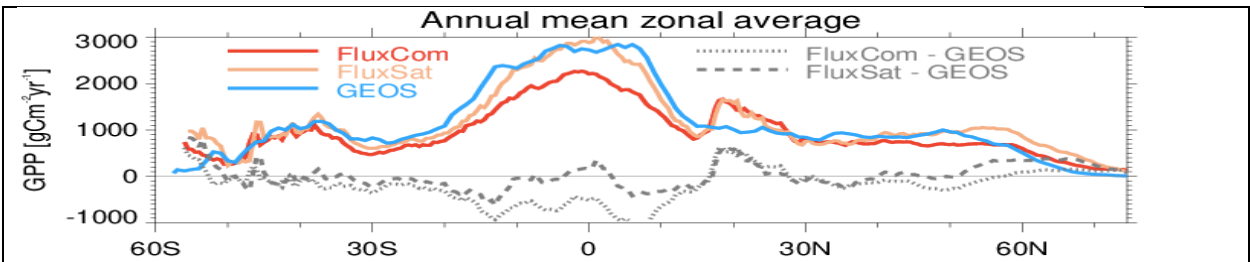


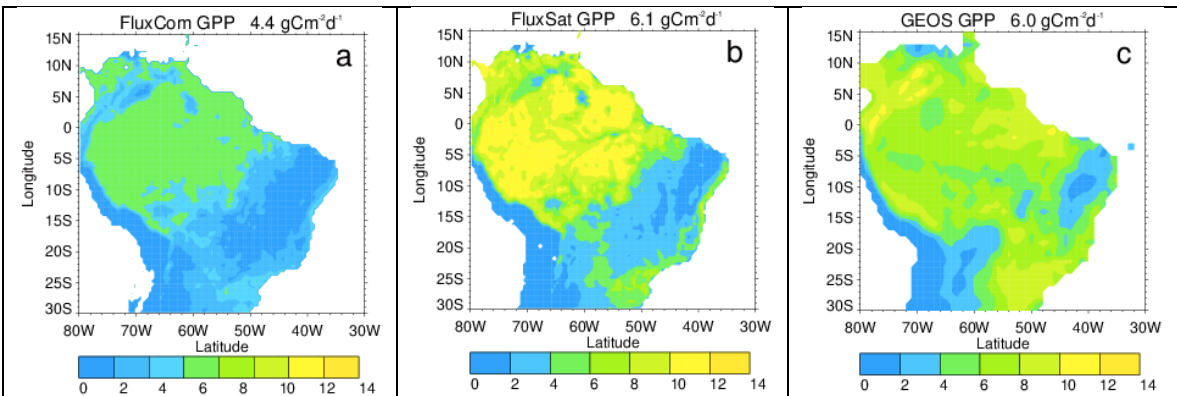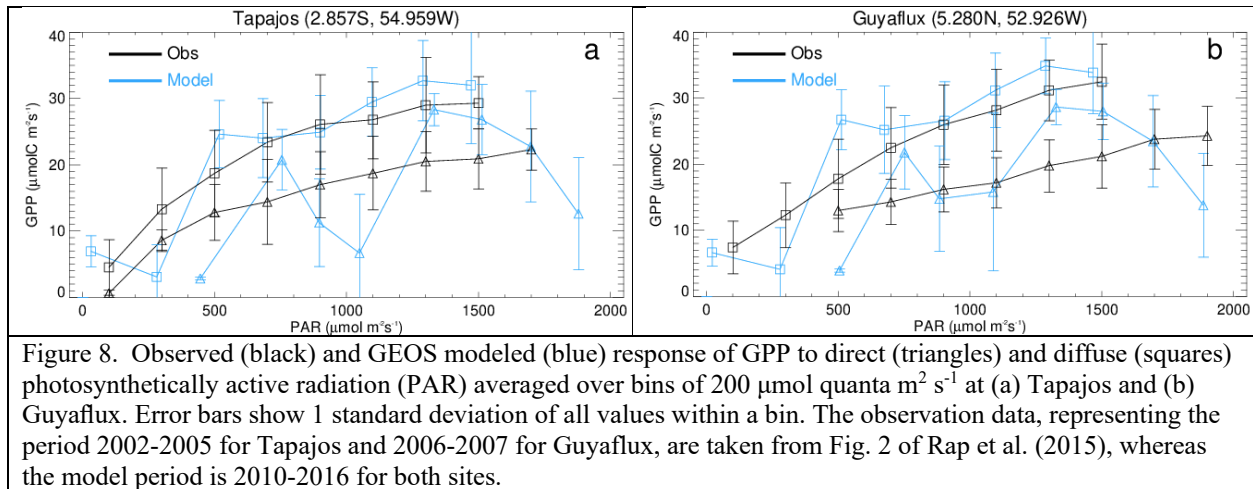Figure 6. Zonal mean of multiyear (2010-2015) average GPP from FluxCom, FluxSat, and GEOS.



Figure 7. The multi-year (2010 – 2015) August – October mean Amazon GPP from (a) FluxCom (Jung et al., 2020), (b) FluxSat ( Joiner et al., 2018) and (c) the GEOS ecosystem simulation with unit of g C m$^{-2}$ day$^{-1}$. The Amazon regional average value is shown in the top.

Figure 7 shows GPP averaged over August to October of 2010-2015 from the two observations-based products and the GEOS simulation. The overall spatial distributions of GEOS GPP (Fig. 7c) over South America show similar spatial pattern to both of the observations-based datasets (Figs. 7a and 7b) with higher values over the eastern part of the domain but lying between the two datasets in other areas.  Over the studied period and the Amazon region, the GEOS GPP is comparable to the FluxSat GPP and is about 35% higher than the FluxCom GPP.

13

501  The seasonality of GPP over the Amazon region from FluxCOM, FluxSat and GEOS during
502  2010-2015 is shown in Fig. S7, and the corresponding time series of monthly means is shown in
503  Fig. S8. During all four seasons, regional FluxCom GPP is the lowest and FluxSat GPP is the
504  highest. All datasets show higher GPP during Nov-Apr than during May-Oct. GEOS multiyear
505  annual average GPP is close to that of FluxSat but is higher than that of FluxCom. Although
506  there are few of observation sites available in FLUXNET 2015 Tier 1
507  (https://fluxnet.org/data/fluxnet2015-dataset/), Joiner et al. (2018) evaluated FluxSat GPP
508  performance around Amazonia using the flux tower measurements, which showed that the high
509  GPP values produced by FluxSat were supported by the flux tower values (Joiner et al., 2018).

510



Figure 8.  Observed (black) and GEOS modeled (blue) response of GPP to direct (triangles) and diffuse (squares) photosynthetically active radiation (PAR) averaged over bins of 200 µmol quanta m$^2$ s$^{-1}$ at (a) Tapajos and (b) Guyaflux. Error bars show 1 standard deviation of all values within a bin. The observation data, representing the period 2002-2005 for Tapajos and 2006-2007 for Guyaflux, are taken from Fig. 2 of Rap et al. (2015), whereas the model period is 2010-2016 for both sites.

511
512  Although the evaluations of global and regional multiyear average GPP conducted above (Figs.
513  5-7) are needed for the examination of the model's fundamental mechanisms including
514  photosynthesis, a more direct evaluation to address the model's accuracy in simulating observed
515  GPP response to changes in diffuse and direct surface radiation is shown in Fig. 8. Following the
516  evaluation approach of Rap et al., (2015), we compared the GPP response to direct and diffuse
517  light at two Amazon sites, Tapajos and Guyaflux. The figure clearly demonstrates that in the
518  model, as in observations, diffuse light is more efficient in stimulating GPP.

519
520      **3.2 Principle of aerosol and cloud impact on surface downward radiation**
521  Radiative responses to aerosols and cloud fields are nonlinear. To better explain the phenomenon
522  examined here – that plant growth increases at low-to-intermediate AOD but decreases at high
523  AOD – we ran the column version of a radiation model, fast-JX (Wild et al., 2000; Bian and
524  Prather, 2002). Fast-JX solves the 8-stream multiple scattering in atmospheric solar radiation
525  transfer for direct and diffuse beams, using the exact scattering phase function and optical depths
526  of atmospheric molecules, aerosols, and clouds, and provides photolytic intensities accurate
527  typically to better than 3%, with worst case errors of no more 10% over a wide range of
528  atmospheric conditions (Wild et al., 2000). No special approximations are needed to treat
529  strongly forward-peaked phase functions. The model has also been evaluated against various
530  other models that participated in an international multi-model comparison for solar fluxes and
531  photolysis calculation (PhotoChem-2008 in Chipperfield et al., 2010) and against the
532  measurements from actinic flux spectroradiometers during the Atmospheric Tomography

533 (ATom) mission (Hair et al., 2018). In the aforementioned evaluations, the fast-JX model is
534 among the models with good performance. The model calculations provide three ratios: (i) CIdir,
535 the ratio of direct downward solar radiation at the surface (Rdir@srf) to the incoming total solar
536 radiation flux at the top of the atmosphere (Rtot@toa), (ii) CIdiff, the ratio of the downward
537 diffuse solar radiation flux (Rdiff@srf) to Rtot@toa, and (iii) CI, the ratio of total solar radiation
538 at the surface to Rtot@toa. Note that all Rs are for the 400-700 nm spectral band. Results for
539 different biomass burning AODs (including the clean air condition, where AOD = 0) for cloud-
540 free conditions are shown in Fig. 9a. When the sky is clear and clean (both cloud-free and
541 without aerosols), roughly 90% of the incoming solar radiation at the top of the atmosphere can
542 reach the plant canopy (i.e., CIdir + CIdiff ≈ 0.9 at BBAOD = 0). The direct solar flux decreases
543 rapidly as the atmosphere becomes polluted (i.e., as BBAOD increases), but for BBAOD levels
544 less than ~0.75, the diffuse solar flux increases. The two are equivalent at AOD ~ 0.5. This light
545 redistribution from direct to diffuse can significantly stimulate plant photosynthesis given that
546 plants use diffuse light more efficiently. Ecosystems could still respond positively to the increase
547 of BBAOD even if the incident diffuse radiation decreases below its peak value, though for some
548 value of BBAOD, the reduction in total radiation will be large enough to overwhelm the impact
549 of increased diffuse radiation, and plant photosynthesis will be lower than that for clean sky
550 conditions.
551
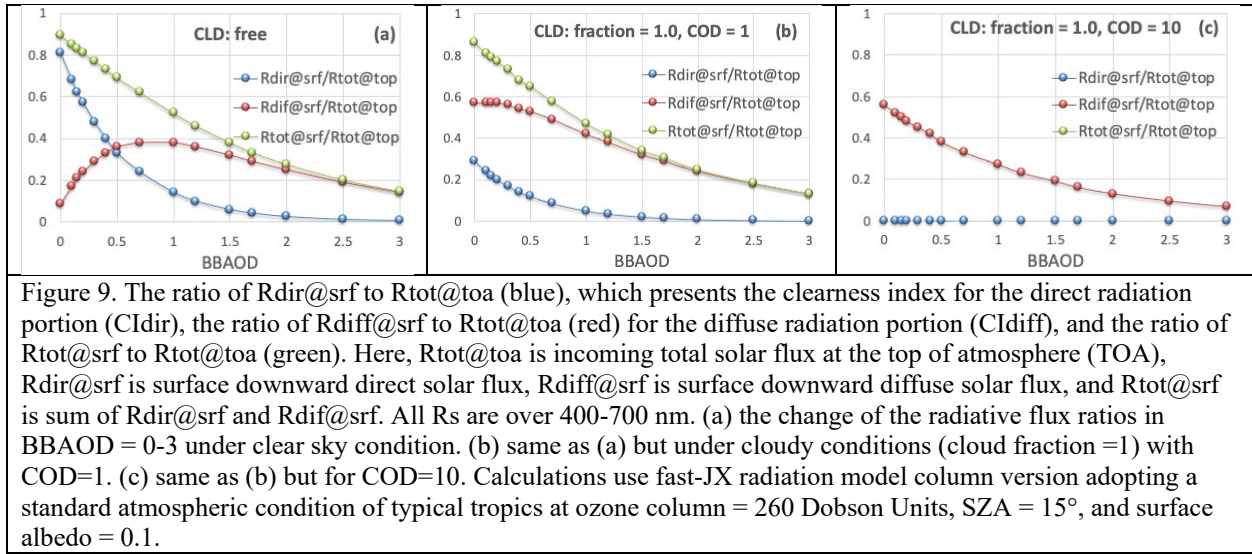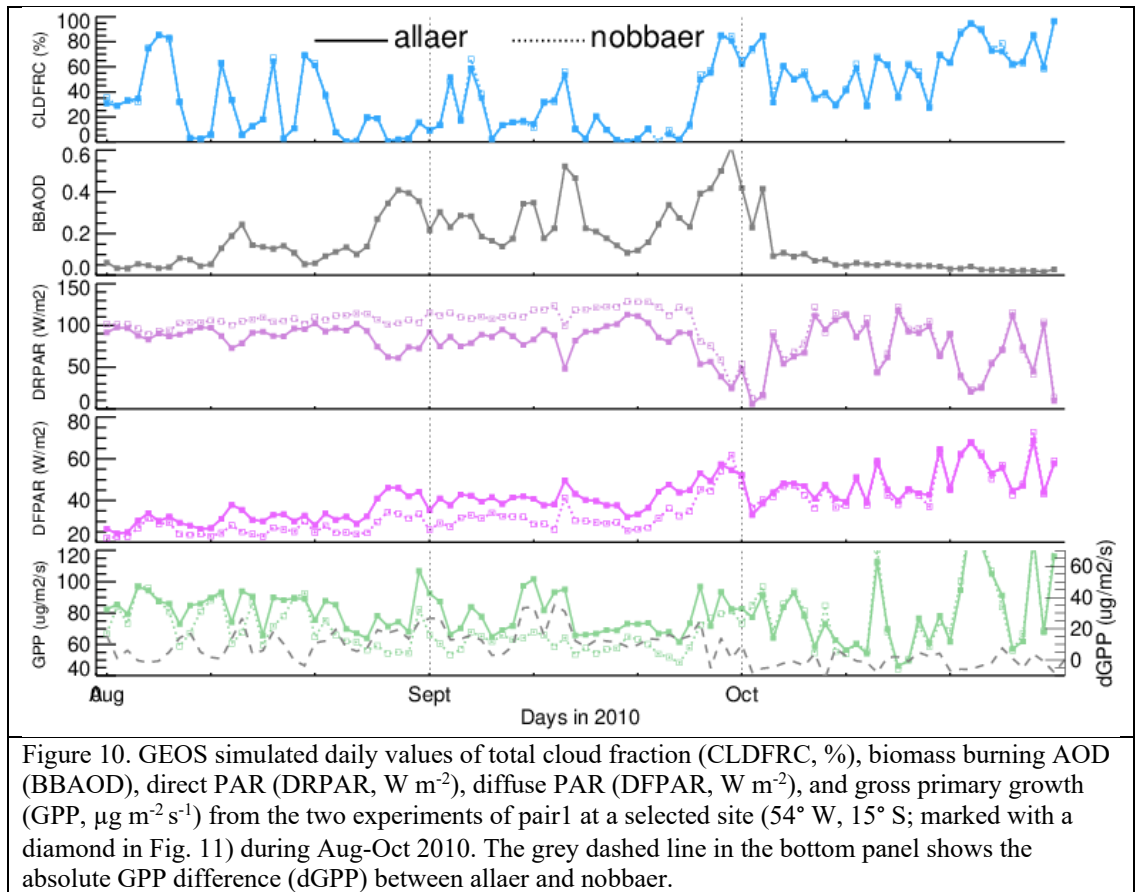


Figure 9. The ratio of Rdir@srf to Rtot@toa (blue), which presents the clearness index for the direct radiation portion (CIdir), the ratio of Rdiff@srf to Rtot@toa (red) for the diffuse radiation portion (CIdiff), and the ratio of Rtot@srf to Rtot@toa (green). Here, Rtot@toa is incoming total solar flux at the top of atmosphere (TOA), Rdir@srf is surface downward direct solar flux, Rdiff@srf is surface downward diffuse solar flux, and Rtot@srf is sum of Rdir@srf and Rdif@srf. All Rs are over 400-700 nm. (a) the change of the radiative flux ratios in BBAOD = 0-3 under clear sky condition. (b) same as (a) but under cloudy conditions (cloud fraction =1) with COD=1. (c) same as (b) but for COD=10. Calculations use fast-JX radiation model column version adopting a standard atmospheric condition of typical tropics at ozone column = 260 Dobson Units, SZA = 15°, and surface albedo = 0.1.

552
553 The Amazon dry season is characterized by high biomass burning aerosol loading combined with
554 low cloud cover, a good match to obtain more diffuse radiation without the loss of too much total
555 radiation. However, as we have pointed out, cloud impacts on radiation typically dominate those
556 of aerosols. To examine this, we repeated the radiation model calculations after adding, at the top
557 of the aerosol layer (~3.5 km), a cloud layer with a cloud fraction of 1.0 and a cloud optical
558 depth (COD) of 1 (Fig. 9b) and 10 (Fig. 9c). The latter COD is close to the mean liquid cloud
559 COD over the Amazon dry season (Fig. 3). The impact on Rdir@srf and Rdiff@srf is quite large
560 even with a very thin overhead cloud (Fig. 9b). Without BBaer, the clouds already produce
561 abundant diffuse light that can reach the surface (i.e., CIdiff > 50%,  as seen in both Fig. 9b-c),
562 while almost shutting down the direct light (i.e., CIdir < 1% in Fig. 9c). Accordingly, for full
563 cloud coverage, a clean sky (i.e., no aerosols) would provide the best conditions for plant growth.
564 When fires start, the diffuse light declines rapidly, reducing the potential for plant growth. At

565 BBAOD ~ 3 the ratios among Fig. 9a-c look similar, that is, essentially very little radiation
566 reaches the surface.

567 The simple examples in Fig. 9 illustrate the complicated responses of direct and diffuse light to
568 the presence of aerosol and cloud. Measurements indicate that plant growth peaks for a clearness
569 index (CI, defined as CIdir+CIdiff) of about 0.4-0.7 for some forest ecosystems (Butt et al.,
570 2010, Letts and Lafleur, 2005). This CI range translates, based on Fig. 9, to a BBAOD range of
571 about 0.3~1.5 in clear sky and 0~0.5 in cloudy-sky conditions.

572
573 **3.3 How the ecosystem responds to the BBaer diffuse radiation fertilization effect**
574



Figure 10. GEOS simulated daily values of total cloud fraction (CLDFRC, %), biomass burning AOD (BBAOD), direct PAR (DRPAR, W m$^{-2}$), diffuse PAR (DFPAR, W m$^{-2}$), and gross primary growth (GPP, µg m$^{-2}$ s$^{-1}$) from the two experiments of pair1 at a selected site (54° W, 15° S; marked with a diamond in Fig. 11) during Aug-Oct 2010. The grey dashed line in the bottom panel shows the absolute GPP difference (dGPP) between allaer and nobbaer.

575
576 We first examine the two experiments in pair1 by taking a close look at the time series of
577 aerosol, cloud, radiation, and ecosystem responses generated at a selected site (54° W, 15° S)
578 during Aug-Oct 2010 (Fig. 10) (site location marked in Fig. 11), with the aim of extending the
579 general understanding gained in section 3.2 to a real case study at a single site in the Amazon.
580 This is an interesting site and period, showing a large DFPAR change (Fig. 11f) and providing a
581 wide variety of conditions for study – the sky alternates between clear and cloudy conditions in
582 August, is relatively clear in September but relatively cloudy in October, and the biomass
583 burning aerosols increase in August, peak in September, and diminish greatly in early October
584 (Fig. 10). During August-September, when the atmosphere experiences biomass burning
585 pollution, the allaer (with BBAOD light fertilizer) and nobbaer (without BBAOD light fertilizer)
586 results differ significantly: DRPAR for allaer (solid line) lies below that for nobbaer (dotted-

16

587    line), while DFPAR and GPP for allaer are generally higher than those for nobbaer. In October,
588    the sky is almost clean (i.e., low BBaer), leading to very similar results for DRPAR, DFPAR,
589    and GPP between the two experiments. Looking closer, we see that the changes of DRPAR,
590    DFPAR, and GPP between allaer and nobbaer are more prominent when the atmosphere has low
591    cloudiness and high aerosol (e.g., at the end of August), confirming both that BBaer does
592    transform some of the direct light at the surface into diffuse light and that plants are more
593    efficient in their use of diffuse light. When both cloudiness and aerosols are high (e.g., at the end
594    of September), the influence of aerosols is overwhelmed by clouds, and the impact of the
595    aerosols on radiation and the ecosystem becomes secondary.
596
597    We now evaluate BB aerosol impacts on radiation and ecosystem fields over the Amazon during
598    August 2010, when the aerosol has its largest impact. Figure 11 shows the simulated Amazon
599    DRPAR, DFPAR, and GPP fields from the two experiments comprising pair1 (nobbaer and
600    allaer). The distribution of DRPAR shows a clear spatial gradient, with low values in the
601    northwest and high values in the southeast, and the spatial pattern of DFPAR shows the reverse
602    pattern. These features are primarily controlled by the cloud distribution (Fig. 3). Comparing the
603    nobbaer and allaer results by calculating field relative change (i.e., (allaer-nobbaer)/allaer), we
604    find that BBaer decreases DRPAR by 16% and increases DFPAR by 10% over the Amazon
605    region, with maximum local changes of up to -50% for DRPAR and 25% for DFPAR.
606    Interestingly, these maxima are not co-located, though the spatial patterns of perturbations do
607    agree with each other. The mismatch in the locations of the maxima in the difference fields
608    implies a nonlinear response of direct and diffuse light to aerosol and cloud particles (see section
609    3.2). In response to the inclusion of BBaer, the Amazon GPP increases by 10%. That is, the
610    increase in GPP stemming from the increase in the diffuse light fraction overwhelms a potential
611    reduction in GPP from a reduction of total PAR.  When we consider all burning seasons over the
612    7-year studied period, the biomass burning aerosol increases DFPAR by 3.8% and decreases
613    DRPAR by 5.4%, allowing it to increase Amazon GPP by 2.6%. However, the 7-year averaged
614    GPP increases by 0.99% (Table 2), which is much less than the value during burning seasons.
615
616    We also examine the multi-year (2010-2016) BBaer impacts on net primary production (NPP),
617    that is, the rate at which carbon is accumulated (GPP) in excess of autotrophic respiration. In
618    essence, NPP can be considered a proxy for the net plant sink of atmospheric carbon. Figure 12
619    shows monthly and long-term averaged NPP over the Amazon Basin from the two experiments
620    comprising pair1. The monthly change of NPP (i.e., dNPP = NPP(allaer) – NPP(nobbaer)) is
621    shown in the figure as a green line. Each year, during the August-September period when BBaer
622    is high and cloudiness is low over the Amazon, BBaer is seen to enhance NPP. The percentage
623    difference of annually-averaged NPP (dNPP/NPP(nobbaer)*100) in % is 4.2, 0.06, 1.9, 0.5, 1.3,
624    1.9, and 1.0 for the seven studied years.  That means the BBaer-induced NPP increases range
625    from 5 Tg C $a^{-1}$ or 0.06% (2011) to 278 Tg C $a^{-1}$ or 4.2% (2010), with a seven-year average of 92
626    Tg C $a^{-1}$ or 1.5%. This is equivalent to storing 92 Tg C annually within the Amazon ecosystem
627    during the studied period. The $CO_2$ fire emission data from the GFED4.1s emission inventory
628    indicate that over this area and time period, fires emit ~250 Tg C $a^{-1}$. The NPP enhancement due
629    to the BBaer-induced diffuse sunlight fertilization thus compensates for about 37% of carbon
630    loss by fires.
631
632
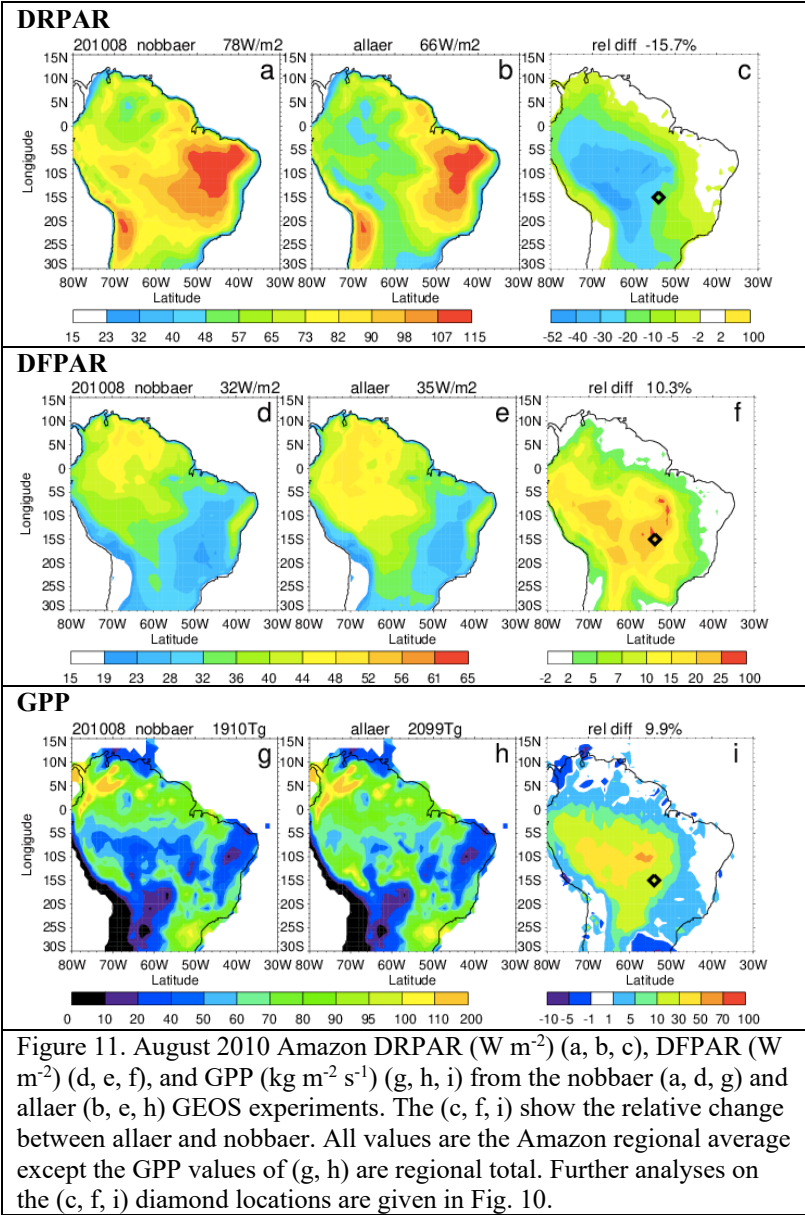
Figure 11. August 2010 Amazon DRPAR (W m$^{-2}$) (a, b, c), DFPAR (W m$^{-2}$) (d, e, f), and GPP (kg m$^{-2}$ s$^{-1}$) (g, h, i) from the nobbaer (a, d, g) and allaer (b, e, h) GEOS experiments. The (c, f, i) show the relative change between allaer and nobbaer. All values are the Amazon regional average except the GPP values of (g, h) are regional total. Further analyses on the (c, f, i) diamond locations are given in Fig. 10.
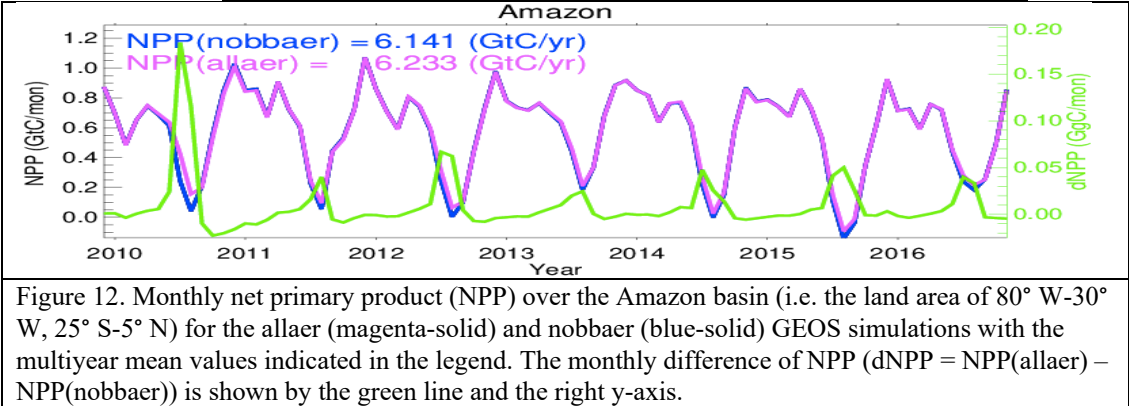


Figure 12. Monthly net primary product (NPP) over the Amazon basin (i.e. the land area of 80° W-30° W, 25° S-5° N) for the allaer (magenta-solid) and nobbaer (blue-solid) GEOS simulations with the multiyear mean values indicated in the legend. The monthly difference of NPP (dNPP = NPP(allaer) – NPP(nobbaer)) is shown by the green line and the right y-axis.

635 To assess how our simulated GPP/NPP response compares with other existing model estimates,
636 we summarize all relevant studies in Table 2. In addition to differences in model formulations of
637 fundamental physical mechanisms, these studies also differ in model simulation configuration
638 (e.g., online vs offline, freeGCM vs Replay), BB emission inventory, and study period. Although
639 our estimates of the increases in NPP across the Amazon region have a wide interannual
640 variation (ranging from 0.5 to 4.2%), our 7-year averaged NPP increase (1.5%) is close to the
641 value (1.4%) reported by Rap et al. (2015). Both studies considered only aerosol DRFE with
642 cloud presence. The NPP can be increased up to 52% in the burning season under clear-sky
643 conditions (Moreira et al., 2017). By accounting for the feedback from aerosol-climate
644 adjustments, the influence of aerosol on GPP/NPP is further increased (Malavelle et al., 2019;
645 Strada et al., 2016).

646

647 Table 2: Summary of model estimation of GPP increase in response to biomass burning aerosol
648 over Amazon Basin

| Study | This work | Malavelle2019 | Moreira2017 | Rap2015 | Strada2016 |
|---|---|---|---|---|---|
| GPP | 1.0% (dir+dif) | | 27% (dir+dif) | 0.7% (dir+dif) | 3.4% (dir+dif+clm)) |
| NPP | 1.5% (dir+dif) | 1.9 to 2.7% (dif+dir+clm) 1.5 to 2.6% (dif) -1.2 to -2.5% (dir) 1.6 to 2.4% (clm) | 52% (dir+dif) | 1.4% (dir+dif) | |
| Period | Annual average over 2010-2016 | Annual average over 30 model years, 2000 climate, | Sept., 2010 under cloud-free condition | Annual average over 1998-2007 | Annual average over 30 model years, 2000 climate |
| Atmospheric Model | GEOS ESM | HadGEM2-ES | BRAMS | | ModelE2 ESM |
| Running mode | replay | freeGCM | Regional model with ICBC from NCEP | offline | freeGCM |
| Vegetation model | Catchment-CN (using LSM4 for photosynthesis) | JULES | JULES | JULES | YiBs |
| Radiation model | RRTMG_SW | SOCRATES | CARMA | A two-stream radiative transfer model (Edwards and Slingo, 1996) | k-distribution approach with various updates (Schmidt et al., 2014) |
| Cloud model | Cloud microphysics model (Barahona et al., 2014) | | | Monthly mean clouds from ISCCP-D2 | a mass flux cumulus parameterization (Del Genio and Yao, 1993) |
| Aerosol model | GOCART | CLASSIC | CCATT | GLOMAP | OMA |
| BB emission | GFED4s | GFEDv2 1997-2006 average | 3BEM | GFED3 | IPCC AR5 |

649 dir, dif, and clm represent for direct radiation, diffuse radiation, and climate adjustment, respectively
650 3BEM: the Brazilian Biomass Burning Emission
651 BRAMS: Brazilian developments on the Regional Atmospheric Modeling System
652 CARMA: the Com-munity Aerosol and Radiation Model for Atmospheres
653 CCATT: a Eulerian transport model suitable to simulate trace gases and aerosols
654 CLASSIC: the Coupled Large-scale Aerosol Simulator for Studies In Climate
655 GLOMAP: The 3-D GLObal Model of Aerosol Processes Model
656 HadGEM2-ES:   The Hadley Centre Global Environment *Model*, version 2-Earth System
657 IPCC AR5: The Intergovernmental Panel on Climate Change Fifth Assessment Report
658 ISCCP-D2: the International Satellite Cloud Climatology Project
659 JULES: the Joint UK Land Environment Sim-ulator v3.0
660 OMA: One-Moment Aerosol,
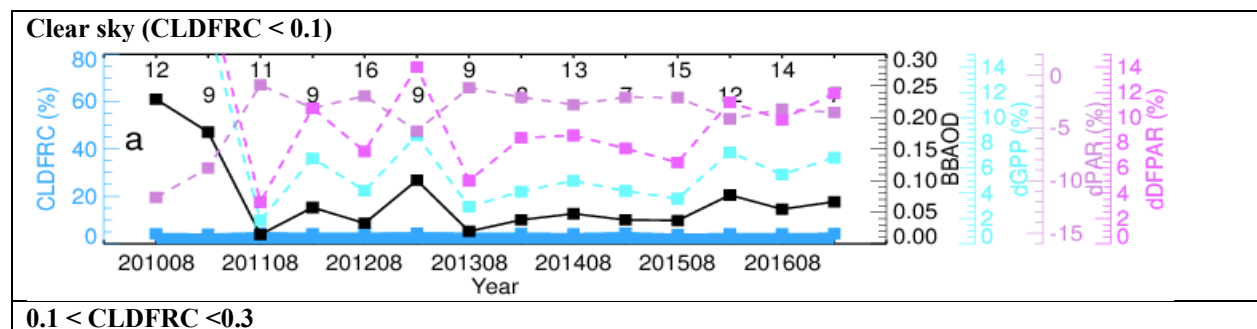661 SOCRATES: Suite Of Community RAdiative Transfer codes based on Edwards and Slingo
662 YIBs: The Yale Interactive Terrestrial Biosphere model

663

## 3.4 How clouds adjust the BBaer diffuse radiation fertilization effect

664
665 Our second objective in this study is to investigate how the presence of clouds modulates the
666 ability of BBaer to affect GPP. We highlight the cloud impact because even at the same biomass

667    burning aerosol optical depth (BBAOD), the surface downward DRPAR and DFPAR can be
668    very different between cloudy and cloud-free conditions (see section 3.2). As mentioned above,
669    the Amazon's so-called "dry season" still features a considerable amount of cloud, and the
670    cloudiness levels vary significantly from year to year. This raises some questions: How do
671    clouds affect the aerosol impact on radiation fields during the Amazon biomass burning season?
672    Could different levels of background clouds have different impacts on the efficacy of the BBaer
673    DRFE? There are two distinctive features in clouds and aerosols that require us to treat them
674    differently in their impact on the radiation flux to the ecosystem. First, like our distinction of
675    natural and anthropogenic aerosols in their impact on air quality and climate, the cloud is a more
676    natural phenomenon, while biomass burning aerosols (BBaer) can be, at least partially,
677    controlled by humans. Second, clouds are much more efficient in controlling both direct and
678    diffuse radiation fields than aerosol (Fig. 9). What is the potential range of the variation of
679    Amazon clouds in burning seasons when the Amazon experiences environments of La Niña,
680    normal years, and El Niño? To what extent does this range of cloud variation adjust the
681    efficiency of "diffuse radiation fertilization effect" under the same emission strategy? These
682    questions were not addressed clearly in previous studies, and we have tried to answer these
683    questions in this study. Here, to quantify the cloud influence, we examine BBaer impacts during
684    clear-sky (cloud cover < 0.1), cloudy-sky (cloud cover 0.1-0.3, 0.3-0.6 and >0.6), and all-sky
685    conditions based on GEOS gridded daily cloud cover over the Amazon region as shown in Fig.
686    13.

688    Generally, the curves for BBAOD (solid black line) and dGPP (dashed light-blue line) are
689    strongly and positively correlated, from R = 77.4% for cloud cover > 0.6 (Fig. 13d) to R > 94.5%
690    for the four other cloudiness conditions (Figs. 13a-c, e). This indicates that interannual changes
691    in dGPP are primarily controlled by interannual fluctuations of biomass burning aerosols. The
692    correlation presumably stems from the fact that biomass burning aerosols increase the diffuse
693    PAR reaching the canopy (dashed pink line) although they decrease the total PAR (dotted purple
694    line) via decreasing direct PAR (Table 3 and Table S1a). This aerosol-radiation-GPP relationship
695    is seen to vary with cloud amount with clouds acting to reduce the aerosol impact; both the
696    diffuse radiation and the GPP show larger changes with BBAOD under clear sky conditions. The
697    overall (i.e., all-sky) aerosol impact on dGPP is similar to that for a cloud coverage of 0.3-0.6,
698    simply because the averaged cloud coverage over the Amazon during the studied period is
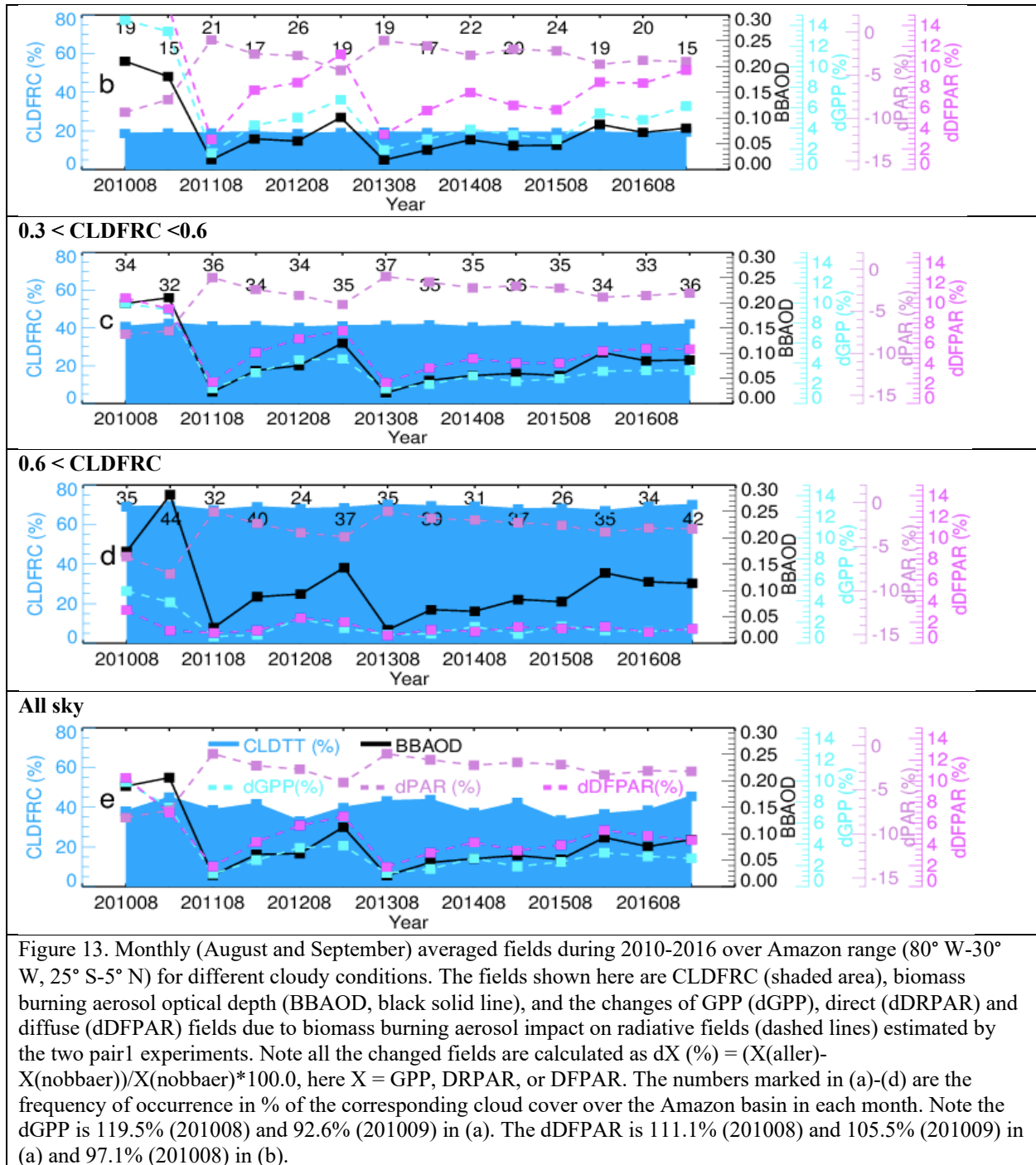699    roughly in that range.



**Clear sky (CLDFRC < 0.1)**

**0.1 < CLDFRC <0.3**

Figure 13. Monthly (August and September) averaged fields during 2010-2016 over Amazon range (80° W-30° W, 25° S-5° N) for different cloudy conditions. The fields shown here are CLDFRC (shaded area), biomass burning aerosol optical depth (BBAOD, black solid line), and the changes of GPP (dGPP), direct (dDRPAR) and diffuse (dDFPAR) fields due to biomass burning aerosol impact on radiative fields (dashed lines) estimated by the two pair1 experiments. Note all the changed fields are calculated as dX (%) = (X(aller)-X(nobbaer))/X(nobbaer)*100.0, here X = GPP, DRPAR, or DFPAR. The numbers marked in (a)-(d) are the frequency of occurrence in % of the corresponding cloud cover over the Amazon basin in each month. Note the dGPP is 119.5% (201008) and 92.6% (201009) in (a). The dDFPAR is 111.1% (201008) and 105.5% (201009) in (a) and 97.1% (201008) in (b).

702

703  Figure 13 and Table S1e show that on an interannual (dry season) basis, the aerosol DRFE
704  differed the most between 2010 and 2011 (i.e., the dGPP was 8.7% in 2010 and 1.8% in 2011).
705  During these two years, the average cloud fractions (CLDFRC) are similar, 42% in 2010 and
706  41% in 2011, but BBAOD decreased significantly, by about 80% from 0.198 in 2010 to 0.042 in
707  2011. Thus, although cloudiness does temper the impact of aerosols on radiation and the
708  ecosystem, the interannual variation of the aerosol DRFE is primarily controlled by variations in
709  biomass burning aerosols (e.g., > 6 times variation of biomass burning emissions and BBAOD,

710   table S1e).  In addition to the detailed information given in Tables S1a-e and S2a-e, we
711   summarize in Table 3 the averaged GPP, DFPAR, DRPAR, CLDFRC, and BBAOD during Aug-
712   Sept, 2011-2016 over the Amazon region in all-sky conditions. Also given in Table 3 is the
713   multi-year (2011-2016) averaged GPP over the Amazon region from all four simulations.
714
715   Table 3. Summary of mean GPP, DRPAR, DFPAR, CLDFRC and BBAOD over Aug-Sept of
716   2011-2016, as well as the relative changes of GPP, DRPAR, DFPAR and CLDFRC within a pair
717   of simulations.

| pair | experiment | GPP | DRPAR | DFPAR | CLDFRC | BBAOD |
|------|-----------|-----|-------|-------|--------|-------|
|      |           | GtC/Amazon | W m$^{-2}$ | W m$^{-2}$ | | |
| Pair1 | allaer | 1.88 | 72.5 | 36.8 | 0.395 | 0.062 |
|       | nobbaer | 1.84 | 76.5 | 35.3 | 0.395 | |
|       | Diff (%) | 2.5 | -5.3 | 4.1 | 0 | |
| Pair2 | callaer | 1.96 | 64.5 | 38.0 | 0.396 | 0.212 |
|       | cnobbaer | 1.83 | 75.4 | 35.1 | 0.395 | |
|       | Diff (%) | 6.9 | -14.4 | 8.2 | 0 | |

718
719   Recall, the pair2 experiments are equivalent to the pair1 experiments except for using the 2010
720   BB emissions for every year during 2011-2016.  By jointly analyzing pair1 and pair 2, we can
721   quantify the impacts of two different sets of BB emissions during the study period. This is, in
722   principle, similar to the method of aerosol radiative forcing (RF) estimation (i.e., estimating
723   aerosol radiative effect (RE) with and without aerosol for present-day (pair1) and pre-industrial
724   (pair2)  conditions and then deriving RF as a difference between the two pair REs). Here we
725   study the sensitivity of the aerosol DRFE to a unit change of AOD. We call it susceptibility of
726   the DRFE to BB aerosols. That is, on a daily basis, the sensitivity of a variable X to a change in
727   the biomass burning AOD is calculated as: $ddX/dAOD = ((dX)_1-(dX)_2)/(AOD_1-AOD_2)$. Here, the
728   X represents GPP, DRPAR, and DFPAR, and the subscripts 1 and 2 represent the pair1 or pair2
729   experiment, respectively.
730
731   ddX/dAOD is computed on a gridded daily basis over August-September of 2011-2016. The
732   calculations are then catalogued according to daily cloud cover fraction – we combine the results
733   within each of 10 cloud fraction bins (0-0.1, 0.1-0.2, …, 0.9-1.0). To examine the maximum
734   impact of interannual cloud change during our study period, the binned ddX/dAOD vs. CLDFRC
735   relationship is also computed separately from daily (August-September) values in 2013 and from
736   corresponding daily values in 2015, as these are the years for which monthly cloud cover is
737   around the maximum (0.44) and minimum (0.35), respectively (Fig. 13 and table S1e).

738   Figure 14 shows the results. An almost linear relationship is seen between the ddX/dAOD values
739   and cloud cover fraction. BB aerosols increase GPP in clear sky conditions (e.g., 29.6 kg m$^{-2}$ s$^{-1}$)
740   but decrease it under full cloudiness conditions (e.g., -5.8 kg m$^{-2}$ s$^{-1}$). The cloud fraction at which
741   BB aerosol switches from stimulating to inhibiting plant growth occurs at ~0.8. Cloud conditions
742   thus not only affect strongly the strength of the aerosol DRFE but can also change the
743   fundamental direction of the effect. The lines produced for the three different study periods are
744   fairly similar, indicating that the relationship of ddX/dAOD to CLDFRC is fairly stable within
745   the range of cloud cover seen over the Amazon during the period of interest. Figure 14 also
746   indicates that the dGPP can change from 18.5 to 15.5 (kg m$^{-2}$ s$^{-1}$) with a unit AOD of burning
747   particles released to the atmosphere under the range of Amazon interannual cloud variation in
748   dry season, which is 0.35 to 0.44 in our study period. In other words, there is ~20% dGPP

749 uncertainty adjusted by background Amazon cloud. Our work demonstrates quantitively the role
750 of clouds in tempering the aerosol diffuse radiation fertilization effect.
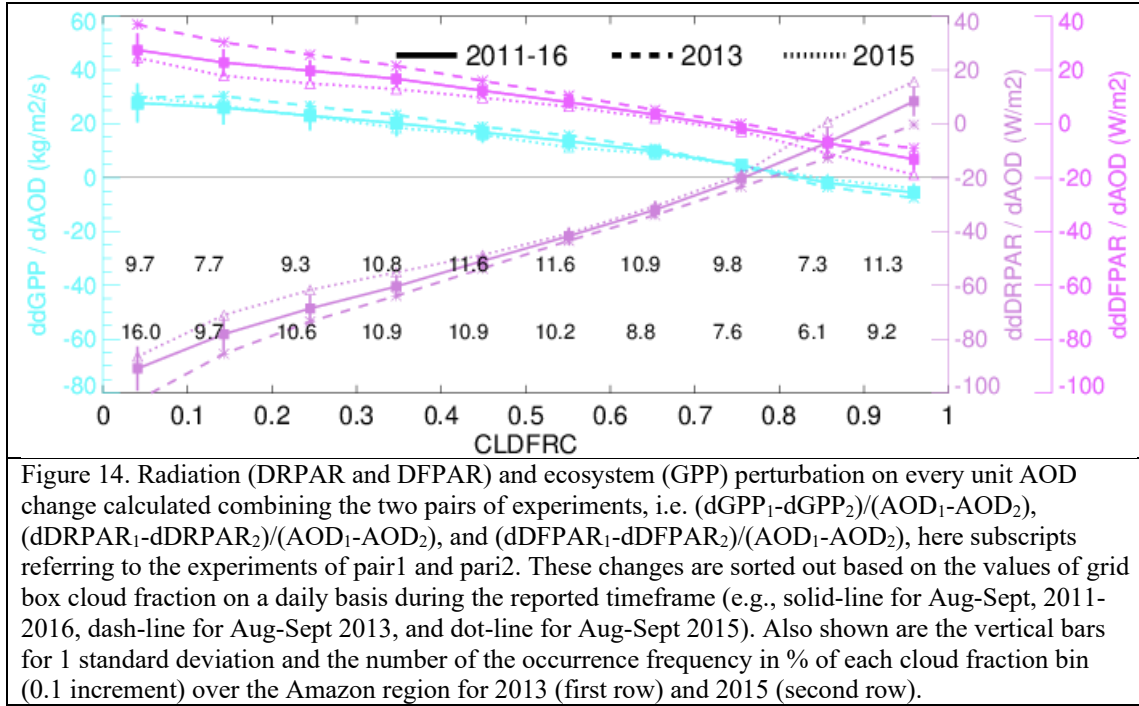751
752



Figure 14. Radiation (DRPAR and DFPAR) and ecosystem (GPP) perturbation on every unit AOD change calculated combining the two pairs of experiments, i.e. $(dGPP_1-dGPP_2)/(AOD_1-AOD_2)$, $(dDRPAR_1-dDRPAR_2)/(AOD_1-AOD_2)$, and $(dDFPAR_1-dDFPAR_2)/(AOD_1-AOD_2)$, here subscripts referring to the experiments of pair1 and pari2. These changes are sorted out based on the values of grid box cloud fraction on a daily basis during the reported timeframe (e.g., solid-line for Aug-Sept, 2011-2016, dash-line for Aug-Sept 2013, and dot-line for Aug-Sept 2015). Also shown are the vertical bars for 1 standard deviation and the number of the occurrence frequency in % of each cloud fraction bin (0.1 increment) over the Amazon region for 2013 (first row) and 2015 (second row).

753
754 **4. Conclusions**
755 We use the NASA GEOS ESM system with coupled aerosol, cloud, radiation, and ecosystem
756 modules to investigate the impact of biomass burning aerosols on plant productivity across the
757 Amazon Basin under the natural background cloud fields experienced during 2010-2016 – a
758 period containing a broad range of cloudiness conditions. We find that the biomass burning
759 aerosol DRFE does stimulate plant growth and has a notable impact on Amazon ecosystem
760 productivity during the biomass burning season (August-September). In the long-term mean, the
761 aerosol light fertilizer increases DFPAR by 3.8% and decreases DRPAR by 5.4%, allowing it to
762 increase Amazon GPP by 2.6% during burning seasons. The 7-year averaged GPP increases by
763 0.99%, which is much less than the value during burning seasons. On a monthly basis, the DRFE
764 can increase GPP by up to 9.9%.  Consequently, biomass burning aerosols increase Amazonia
765 yearly NPP by 1.5% on average, with yearly increases ranging from 0.06% to 4.2% over the
766 seven years studied. This 1.5% NPP enhancement (or ~92 Tg C $a^{-1}$) is equivalent to ~37% of the
767 carbon loss due to Amazon fires.
768
769 The aerosol DRFE is strongly dependent on the presence of clouds, much stronger in clear sky
770 conditions and decreases with the increase of cloudiness. A fairly robust linear relationship is
771 found between cloud cover fraction and the sensitivity of radiation and GPP change to a change
772 in biomass burning AOD. BB aerosols stimulate plant growth under clear-sky conditions but
773 suppress it under full cloudiness conditions. Over the Amazon region within our study period,
774 the cloud fraction at which a unit AOD switches from stimulating to inhibiting plant growth
775 occurs at ~0.8. Note, however, that while our results show a clear sensitivity of the aerosol

776 DRFE to cloudiness, interannual variations in the aerosol light fertilizer's overall effectiveness
777 are controlled primarily by interannual variations in biomass burning aerosols during our studied
778 period because biomass burning AOD can vary by a factor of 6 from year to year. The associated
779 large variations in BBAOD are inevitably propagated to the radiation and ecosystem fields.
780 Overall, our work indicates that feedbacks between aerosols, radiation, and the ecosystem need
781 to be performed in the context of an atmospheric environment with a cloud presence.
782
783 This study examines the potential for the biomass burning aerosol DRFE to stimulate growth in
784 unburned forest over the Amazon basin. The net feedback of Amazon fires on the Amazon
785 biome is still an open question. Some changes, such as increasing atmospheric $CO_2$ and aerosols,
786 serve as forest fertilizers, whereas others, such as increasing $O_3$ pollution levels and the
787 deposition of smoke particles on plant leaves, reduce plant photosynthesis. On top of this, fires
788 also induce changes in meteorological fields (e.g., temperature, precipitation, clouds) that can
789 affect plant growth (Malavelle et al., 2019; Strada and Unger, 2016; Unger et al., 2017). More
790 efforts are needed to investigate the ecosystem effect of Amazon fires by integrating all these
791 potential factors.
792

807

808 **Data Availability:**
809 All of the observational data used in this study are publicly accessible, e.g., AERONET
810 (https://aeronet.gsfc.nasa.gov), CERES-EBAF (https://ceres.larc.nasa.gov/data/), FluxCom
811 (http://www.fluxcom.org), FluxSat (https://avdc.gsfc.nasa.gov), and GoAmazon
812 (https://www.arm.gov/research/campaigns/amf2014goamazon). The GEOS model results can be
813 provided by contacting with the corresponding author.
814

815 **Author contributions:**
816 H.B. took an overall responsible for the experiment design, model simulation, and data analysis.
817 E.L., R. D. K., S. P. M., and F. Z. contributed to the ecosystem study, D. O. B. contributed to the
818 cloud study, M. C., P. R. C., A. S. D, M. E. M., and H. Y. contributed to the aerosol study and
819 the model-observation comparison, P. N. contribute to the radiation study, and J. S. provided the
820 GoAmazon results. All authors contributed to the paper writing.
821

822
**References:**
823
824 Abdul-Razzak, H. and Ghan, S.: A parameterisation of aerosol activation 2. Multiple aerosol types, J.
825     Geophys. Res., 105, 6837–6844, 2000.
826 Barahona, D. and Nenes, A.: Parameterizing the competition be- tween homogeneous and heterogeneous
827     freezing in cirrus cloud formation – monodisperse ice nuclei, Atmos. Chem. Phys., 9, 369–381,
828     doi:10.5194/acp-9-369-2009, 2009
829 Barahona, D., Molod, A., Bacmeister, J., Nenes, A., Gettelman, A., Morrison, H., Phillips, V., and
830     Eichmann, A.: Development of two-moment cloud microphysics for liquid and ice within the NASA
831     Goddard Earth Observing System Model (GEOS-5), Geoscientific Model 10 Development, 7, 1733–
832     1766, 2014.
833 Bian, H., and Prather, M. J.: Accurate simulation of stratospheric photolysis in global chemical model. J.
834     Atmos. Chem., 41, 281-296, 2002.
835 Bian, H., Chin, M., Kawa, S. R., Yu, H., Diehl, T.: Multi-scale carbon monoxide and aerosol correlations
836     from MOPITT and MODIS satellite measurements and GOCART model: implication for their
837     emissions and atmospheric evolutions, J. Geophys. Res., 115, D07302, doi:10.1029/2009JD012781,
838     2010.
839 Bian, H., Colarco, P., Chin, M., Chen, G,, Rodriguez, J. M., Liang, Q., Blake, D., Chu, D. A., da Silva,
840     A., Darmenov, A. S., Diskin, G., Fuelberg, H. E., Huey, G., Kondo, Y., Nielsen, J. E., Pan, X., and
841     Wisthaler, A.: Source attributions of pollution to the western Arctic during the NASA ARCTAS field
842     campaign, Atmos. Chem. Phys., 13, 4707–4721, 2013.
843 Bian, H., Chin, M., Hauglustaine, D. A., Schulz, M., Myhre, G., Bauer, S. E., Lund, M. T., Karydis, V.
844     A., Kucsera, T. L., Pan, X., Pozzer, A., Skeie, R. B., Steenrod, S. D., Sudo, K., Tsigaridis, K.,
845     Tsimpidi, A. P., and Tsyro, S. G.: Investigation of global particulate nitrate from the AeroCom phase
846     III experiment Atmos. Chem. Phys., 17, 12911–12940 (https://www.atmos-chem-
847     phys.net/17/12911/2017/) 2017.
848 Bian, H., Froyd, K., Murphy, D. M., Dibb, J., Darmenov, A., Chin, M., Colarco, P. R., da Silva, A.,
849     Kucsera, T. L., Schill, G., Yu, H., Bui, P., Dollner, M., Weinzierl, B., and Smirnov, A.:
850     Observationally constrained analysis of sea salt aerosol in the marine atmosphere, Atmos. Chem.
851     Phys., 19, 10773–10785, https://doi.org/10.5194/acp-19-10773-2019, 2019.
852 Breen, K. H., Barahona, D., Yuan, T., Bian, H., and James, S. C.: Effect of volcanic emissions
853     on clouds during the 2008 and 2018 Kilauea degassing events, https://doi.org/10.5194/acp-
854     2020-979, 2020.
855 Butt, N., M. New, Y. Malhi, A. C. Lola da Costa, P. Oliveira, and J. E. Silva-Espejo: Diffuse radiation
856     and cloud fraction relationships in two contrasting Amazonian rainforest sites, Agric. For. Meteorol.,
857     150(3), 361–368, 2010.
858 Carn, S., Fioletov, V., McLinden, C., Li, C., and Krotkov, N. A.: A decade of global volcanic
859     $SO_2$ emissions measured from space. *Sci Rep* **7,** 44095, https://doi.org/10.1038/srep44095, 2017.
860 Chin, M., T. Diehl, O. Dubovik, T. F. Eck, B. N. Holben, A. Sinyuk, and D. G. Streets: Light absorption
861     by pollution, dust and biomass burning aerosols: A global model study and evaluation with
862     AERONET data, Ann. Geophys., 27, 3439-3464, 2009.
863 Chin, M., Diehl, T., Tan, Q., Prospero, J. M., Kahn, R. A., Remer, L. A., Yu, H., Sayer, A. M., Bian, H.,
864     Geogdzhayev, I. V., Holben, B. N., Howell, S. G., Huebert, B. J., Hsu, N. C., Kim, D., Kucsera, T. L.,
865     Levy, R. C., Mishchenko, M. I., Pan, X., Quinn, P. K., Schuster, G. L., Streets, D. G., Strode, S. A.,
866     Torres, O., and Zhao, X.-P.: Multi-decadal aerosol variations from 1980 to 2009: a perspective from
867     observations and a global model, Atmos. Chem. Phys., 14, 3657–3690, https://doi.org/10.5194/acp-
868     14-3657-2014, 2014.
869 Chipperfield M., Kinnison,D., Bekki S., Bian H., Brühl, C., Canty T., Cionni I., Dhomse S., Froidevaux
870     L., Fuller R., Müller R., Prather M., Salawitch R., Santee M., Tian W., Tilmes S.: Stratospheric
871     Cheistry (Chapter 6) in SPARC Report on the Evaluation of Chemistry-Climate Models, SPARC

CCMVal, V. Eyring, T. G. Shepherd, D. W. Waugh (Eds.), SPARC Report No. 5, pp.191-252, WCRP-132, WMO/TD-No. 1526, http://www.atmosp.physics.utoronto.ca/SPARC, 2010.

Colarco, P. R., A. da Silva, M. Chin, T. Diehl: Online simulations of global aerosol distributions in the NASA GEOS-4 model and comparisons to satellite and ground-based aerosol optical depth, J. Geophys. Res., 115, D14207, doi:10.1029/2009JD012820, 2010.

Colarco, P. R., Gassó., S., Ahn, C., Buchard, V., Dasilva, A. M., & Torres, O. (2017). Simulation of the Ozone Monitoring Instrument aerosol index using the NASA Goddard Earth Observing System aerosol reanalysis products. Atmospheric Measurement Techniques. https://doi.org/10.5194/amt-10-4121-2017.

Cirino, G. G., R. A. F. Souza, D. K. Adams, and P. Artaxo, The effect of atmospheric aerosol particles and clouds on net ecosystem exchange in the Amazon, Atmos. Chem. Phys., 14, 6523–6543, www.atmos-chemphys, 2014.

Del Genio, A. D., M.-S. Yao, and J. Jonas (2007), Will moist convection be stronger in a warmer climate?, Geophys. Res. Lett., 34, L16703, doi:10.1029/2007GL030525.

Doughty, C. E., M. G. Flanner, and M. L. Goulden (2010), Effect of smoke on subcanopy shaded light, canopy temperature, and carbon dioxide uptake in an Amazon rainforest, Global Biogeochem. Cycles, 24, GB3015, doi:10.1029/2009GB003670.

Doughty, C.E., Metcalfe, D.B., Girardin, C.A.J., Farfan-Amezquita, F., Galiano Cabrera, D., Huaraca Huasco, W., Silva-Espejo, J. E., Araujo-Murakami, A., da Costa, M. C., Rocha, W., Feldpausch, T. R., Mendoza, A. L. M., da Costa, A. C. L., Meir, P., Phillips, O. L., and Malhi, Y.: Drought impact on forest carbon dynamics and fluxes in Amazonia. Nature, 519:78–82, 2015.

Doughty, Russell, Philipp Köhler, Christian Frankenberg, Troy S. Magney, Xiangming Xiao, Yuanwei Qin, Xiaocui Wu, Berrien Moore. TROPOMI reveals dry-season increase of solar-induced chlorophyll fluorescence in the Amazon forest. Proceedings of the National Academy of Sciences, 2019; 201908157 DOI: 10.1073/pnas.1908157116.

Dubovik, O., Smirnov, A., Holben, B. N., King, M. D., Kauf- man, Y. J., Eck, T. F., and Slutsker, I.: Accuracy assessments of aerosol optical properties retrieved from AERONET Sun and sky-radiance measurements, J. Geophys. Res., 105, 9791–9806, 2000.

Dubovik, O., Holben, B. N., Eck, T. F., Smirnov, A., Kaufman, Y. J., King, M. D., Tanré, D., and Slutsker, I.: Variability of ab- sorption and optical properties of key aerosol types observed in worldwide locations, J. Atmos. Sci., 59, 590–608, 2002.

Edwards, J. M., and Slingo, A.: Studies with a flexible new radiation code. 1: Choosing a configuration for a large-scale model, W. J. R. Meteorol. Soc., 122(531), 689-719, 1996.

Ezhova, E., Ylivinkka, I., Kuusk, J., Komsaare, K., Vana, M., Krasnova, A., Noe, S., Arshinov, M., Belan, B., Park, S. B., Lavrič, J. V., Heimann, M., Petäjä, T., Vesala, T., Mammarella, I., Kolari, P., Bäck, J., Rannik, Ü., Kerminen, V. M., & Kulmala, M. (2018). Direct effect of aerosols on solar radiation and gross primary production in boreal and hemiboreal forests. *Atmospheric Chemistry and Physics*, **18**(24), 17,863– 17,881. https://doi.org/10.5194/acp-18-17863-2018.

Feldpausch, T. R., Phillips, O. L., Brienen, R. J. W., Gloor, E., Lloyd, J., Lopez-Gonzalez, G., Monteagudo-Mendoza, A., Malhi, Y., Alarcón, A., Álvarez Dávila, E., Alvarez-Loayza, P., Andrade, A., Aragão, L. E. O. C., Arroyo, L., Aymard C., G. A., Baker, T. R., Baraloto, C., Barroso, J., Bonal, D., Castro, W., Chama, V., Chave, J., Domingues, T. F., Fauset, S., Groot, N., Honorio Coronado, E., Laurance, S., Laurance, W. F., Lewis, S. L., Licona, J. C., Marimon, B. S., Marimon-Junior, B. H., Mendoza Bautista, C., Neill, D. A., Oliveira, E. A., Oliveira dos Santos, C., Pallqui Camacho, N. C., Pardo-Molina, G., Prieto, A., Quesada, C. A., Ramírez, F., Ramírez-Angulo, H., Réjou-Méchain, M., Rudas, A., Saiz, G., Salomão, R. P., Silva-Espejo, J. E., Silveira, M., ter Steege, H., Stropp, J., Terborgh, J., Thomas-Caesar, R., van der Heijden, G. M. F., Vásquez Martinez, R., Vilanova, E., & Vos, V. A. (2016). Amazon forest response to repeated droughts. Global Biogeochemical Cycles, 30, 964– 982. https://doi.org/10.1002/2015GB005133.

Feng, Y., Chen, D. & Zhao, X. Estimated long-term variability of direct and diffuse solar radiation in North China during 1959–2016. Theor Appl Climatol 137, 153–163 (2019). https://doi.org/10.1007/s00704-018-2579-1

Fountoukis, C. and Nenes, A.: Continued development of a cloud droplet formation parameterization for global climate models, J. Geophys. Res., 110, D11212, doi:10.1029/2004JD005591, 2005.

Gelaro, R., McCarty, W., Suárez, M. J., Todling, R., Molod, A., Takacs, L., et al. (2017). The Modern-Era Retrospective Analysis for Research and Applications, Version 2 (MERRA-2). Journal of Climate, 30(14), 5419–5454. https://doi.org/10.1175/JCLI-D-16-0758.1

Gu, L. H., D. D. Baldocchi, S. C. Wofsy, J. W. Munger, J. J. Michalsky, S. P. Urbanski, and T. A. Boden (2003), Response of a deciduous forest to the Mount Pinatubo eruption: Enhanced photosynthesis, Science, 299(5615), 2035–2038.

Guenther, A. B., X. Jiang, C. L. Heald, T. Sakulyanontvittaya, T. Duhl, L. K. Emmons and X. Wang (2012). "The Model of Emissions of Gases and Aerosols from Nature version 2.1 (MEGAN2.1): an extended and updated framework for modeling biogenic emissions." Geosci. Model Dev. 5(6): 1471-1492.

Hall, S. R., Ullmann, K., Prather, M. J., Flynn, C. M., Murray, L. T., Fiore, A. M., Correa, G., Strode, S. A., Steenrod, S. D., Lamarque, J.-F., Guth, J., Josse, B., Flemming, J., Huijnen, V., Abraham, N. L., and Archibald, A. T.: Cloud impacts on photochemistry: building a climatology of photolysis rates from the Atmospheric Tomography mission, Atmos. Chem. Phys., 18, 16809–16828, https://doi.org/10.5194/acp-18-16809-2018, 2018.

Hemes, K. S., Verfaillie, J., and Baldocchi, D. D.: Wildfire-Smoke Aerosols Lead to Increased Light Use Efficiency Among Agricultural and Restored Wetland Land Uses in California's Central Valley, J. Geophys. Res.-Biogeo., 125, e2019JG005380, https://doi.org/10.1029/2019jg005380, 2020.

Hodzic A. and Jimenez J.L. (2011), Modeling anthropogenically controlled secondary organic aerosols in a megacity: a simplified framework for global and climate models. Geosci. Model. Dev., 4, 901-917, doi:10.5194/gmd-4-901-2011.

Huete, A. R., K. Didan, Y. E. Shimabukuro, P. Ratana, S. R. Saleska, L. R. Hutyra, W. Yang, R. R. Nemani, and R.

Myneni (2006), Amazon rainforests green-up with sunlight in dry season, Geophys. Res. Lett., 33, L06405, doi:10.1029/2005GL025583.

Iacono, M.J., J.S. Delamere, E.J. Mlawer, M.W. Shephard, S.A. Clough, and W.D. Collins, Radiative forcing by long-lived greenhouse gases: Calculations with the AER radiative transfer models, J. Geophys. Res., 113, D13103, doi:10.1029/2008JD009944, 2008.

Joiner, J., Yoshida, Y., Zhang, Y., Duveiller, G., Jung, M., Lya- pustin, A., Wang, Y., and Tucker, J. C.: Estimation of Terres- trial Global Gross Primary Production (GPP) with Satellite Data- Driven Models and Eddy Covariance Flux Data, Remote Sens., 10, 1346, https://doi.org/10.3390/rs10091346, 2018.

Jung, M., Schwalm, C., Migliavacca, M., Walther, S., Camps-Valls, G., Koirala, S., et al. (2020). Scaling carbon fluxes from eddy covariance sites to globe: synthesis and evaluation of the FLUXCOM approach. *Biogeosciences*, *17*(5), 1343–1365. https://doi.org/10.5194/bg-17-1343-2020

Kato, S., N. Loeb, F. G. Rose, D. R. Doelling, D. A. Rutan, T. E. Caldwell, L. Yu, and R. A. Weller (2013), Surface irradiances consistent with CERES-derived top-of-atmosphere shortwave and longwave irradiances. J. Climate, 26, 2719–2740, doi:10.1175/JCLI-D-12-00436.1.

Keppel-Aleks, G., and Washenfelder, R.A. 2016. "The effect of atmospheric sulfate reductions on diffuse radiation and photosynthesis in the United States during 1995–2013." Geophysical Research Letters, Vol. 43(No. 18): pp. 9984–9993. doi:10.1002/2016GL070052.

Kim, P. S., Jacob, D. J., Fisher, J. A., Travis, K., Yu, K., Zhu, L., Yantosca, R. M., Sulprizio, M. P., Jimenez, J. L., Campuzano-Jost, P., Froyd, K. D., Liao, J., Hair, J. W., Fenn, M. A., Butler, C. F., Wagner, N. L., Gordon, T. D., Welti, A., Wennberg, P. O., Crounse, J. D., St. Clair, J. M., Teng, A. P., Millet, D. B., Schwarz, J. P., Markovic, M. Z., and Perring, A. E.: Sources, seasonality, and trends

975 of southeast US aerosol: an integrated analysis of surface, aircraft, and satellite observations with the
976 GEOS-Chem chemical transport model, Atmos. Chem. Phys., 15, 10411–10433,
977 https://doi.org/10.5194/acp-15-10411-2015, 2015.
978 Koster, R. D., M. J. Suarez, A. Ducharne, M. Stieglitz, and P. Kumar, 2000: A catchment-based approach
979 to modeling land surface processes in a general circulation model: 1. Model structure. J. Geophys.
980 Res., 105, 24 809–24 822, doi:10.1029/2000JD900327.
981 Koster, R. D., and G. K. Walker (2015), Interactive vegetation phenology, soil moisture, and monthly
982 temperature forecasts, J. Hydrometeorol., 16, 1456–1465, doi:10.1175/JHM-D-14-0205.1.
983 Laurance, W.F. 1999. Gaia's lungs: Are rainforests inhaling Earth's excess carbon dioxide? Natural
984 History (April), p. 96.
985 Lawrence, D. M., Fisher, R. A., Koven, C. D., Oleson, K. W., Swenson, S. C., Bonan, G., et al. (2019).
986 The Community Land Model version 5: Description of new features, benchmarking, and impact of
987 forcing uncertainty. Journal of Advances in Modeling Earth Systems,
988 https://doi.org/10.1029/2018MS001583.
989 Min S. Lee, David Y. Hollinger, Trevor F. Keenan, Andrew P. Ouimette, Scott V. Ollinger, Andrew D.
990 Richardson, Model-based analysis of the impact of diffuse radiation on $CO_2$ exchange in a temperate
991 deciduous forest, Agricultural and Forest Meteorology, 249, 377-389,
992 https://doi.org/10.1016/j.agrformet.2017.11.016, 2018.
993 Letts, M. G., P.M. Lafleur, and N.T. Roulet, On the relationship between cloudiness and net ecosystem
994 carbon dioxide exchange in a peatland ecosystem Ecoscience, 12 (1) (2005), pp. 53–59.
995 Li, T. and Q. Yang, Advantages of diffuse light for horticultural production and perspectives for further
996 research. Front Plant Sci. 2015; 6: 704, published online 2015 Sep 4. doi: 10.3389/fpls.2015.00704.
997 Li, W., R. Fu, and R. E. Dickinson (2006), Rainfall and its seasonality over the Amazon in the 21st
998 century as assessed by the coupled models for the IPCC AR4, J. Geophys. Res., 111, D02111,
999 doi:10.1029/2005JD006355.
1000 Malavelle, F. F., Haywood, J. M., Mercado, L. M., Folberth, G. A., Bellouin, N., Sitch, S., and Artaxo, P.:
1001 Studying the impact of biomass burning aerosol radiative and climate effects on the Amazon
1002 rainforest productivity with an Earth system model, Atmos. Chem. Phys., 19, 1301–1326,
1003 https://doi.org/10.5194/acp-19-1301-2019, 2019.
1004 Martin, S. T., Artaxo, P., Machado, L. A. T., Manzi, A. O., Souza, R. A. F., Schumacher, C., Wang, J.,
1005 Andreae, M. O., Barbosa, H. M. J., Fan, J., Fisch, G., Goldstein, A. H., Guenther, A., Jimenez, J. L.,
1006 Pöschl, U., Silva Dias, M. A., Smith, J. N., and Wendisch, M.: Introduction: Observations and
1007 Modeling of the Green Ocean Amazon (GoAmazon2014/5), Atmos. Chem. Phys., 16, 4785–4797,
1008 https://doi.org/10.5194/acp-16-4785-2016, 2016.
1009 Mercado, L. M., N. Bellouin, S. Sitch, O. Boucher, C. Huntingford, M. Wild, and P. M. Cox (2009),
1010 Impact of changes in diffuse radiation on the global land carbon sink, Nature, 458(7241), 1014–1017.
1011 Molod, A., L. Takacs, M. Suarez, J. Bacmeister, I.-S. Song, and A. Eichmann, 2012. The GEOS-5
1012 Atmospheric General Circulation Model: Mean Climate and Development from MERRA to Fortuna.
1013 Technical Report Series on Global Modeling and Data Assimilation, 28, 2012
1014 (http://gmao.gsfc.nasa.gov/ pubs/docs/Molod484.pdf).
1015 Molod, A., Takacs, L., Suarez, M., and Bacmeister, J.: Development of the GEOS-5 atmospheric general
1016 circulation model: evolu- tion from MERRA to MERRA2, Geoscientific Model Development, 8,
1017 1339–1356, https://doi.org/10.5194/gmd-8-1339-2015, https: //www.geosci-model-
1018 dev.net/8/1339/2015/, 2015.
1019 Moreira, D. S., Longo, K. M., Freitas, S. R., Yamasoe, M. A., Mer- cado, L. M., Rosário, N. E., Gloor, E.,
1020 Viana, R. S. M., Miller, J. B., Gatti, L. V., Wiedemann, K. T., Domingues, L. K. G., and Correia, C.
1021 C. S.: Modeling the radiative effects of biomass burning aerosols on carbon fluxes in the Amazon
1022 region, Atmos. Chem. Phys., 17, 14785–14810, https://doi.org/10.5194/acp-17- 14785-2017, 2017.
1023 Murphy, D. M., Froyd, K. D., Bian, H., Brock, C. A., Dibb, J. E., DiGangi, J. P., Diskin, G., Dollner, M.,
1024 Kupc, A., Scheuer, E. M., Schill, G. P., Weinzierl, B., Williamson, C. J., and Yu, P.: The distribution

1025       of sea-salt aerosol in the global troposphere, Atmos. Chem. Phys., 19, 4093-4104,
1026       https://doi.org/10.5194/acp-19-4093-2019, Apr., 2019.
1027 Myneni, R., Knyazikhin, Y., Park, T. (2015). MOD15A2H MODIS Leaf Area Index/FPAR 8-Day L4
1028       Global 500m SIN Grid V006. NASA EOSDIS Land Processes DAAC.
1029       http://doi.org/10.5067/MODIS/MOD15A2H.006 (Terra) and
1030       http://doi.org/10.5067/MODIS/MYD15A2H.006 (Aqua).
1031 Napstad, D., C. M. Stickler, B. Soares-Filho, and F. Merry, Interactions among Amazon land use, forests
1032       and climate: prospects for a near-term forest tipping point, Philos Trans R Soc Lond B Biol Sci.;
1033       363(1498): 1737–1746, doi: 10.1098/rstb.2007.0036, May 27, 2008.
1034 Nepstad DC, Stickler CM, Filho BS, Merry F. Interactions among Amazon land use, forests and climate:
1035       prospects for a near-term forest tipping point. Philos Trans R Soc Lond B Biol Sci. 2008;
1036       363(1498):1737-1746. doi:10.1098/rstb.2007.0036.
1037 Ng, N. L., S. C. Herndon, A. Trimborn, M. R. Canagaratna, P. L. Croteau, T. B. Onasch, D. Sueper, D. R.
1038       Worsnop, Q. Zhang, Y. L. Sun and J. T. Jayne (2011). "An Aerosol Chemical Speciation Monitor
1039       (ACSM) for Routine Monitoring of the Composition and Mass Concentrations of Ambient Aerosol."
1040       Aerosol Science and Technology 45(7): 780-794.
1041 Niyogi, Dev ; Chang, Hsin-I ; Saxena, V. K ; Holt, Teddy ; Alapaty, Kiran ; Booker, Fitzgerald ; Chen,
1042       Fei ; Davis, Kenneth J ; Holben, Brent ; Matsui, Toshihisa ; Meyers, Tilden ; Oechel, Walter C ;
1043       Pielke Sr, Roger A ; Wells, Randy ; Wilson, Kell ; Xue, Yongkang: Direct observations of the effects
1044       of aerosol loading on net ecosystem $CO_2$ exchanges over different landscapes, Geophys. Res. Lett.,
1045       31, L20506, doi:10.1029/2004GL020915, 2004.
1046 Oliveira, P. H. F., P. Artaxo, C. Pires, S. De Lucca, A. Procopio, B. Holben, J. Schafer, L. F. Cardoso, S.
1047       C. Wofsy, and H. R. Rocha (2007), The effects of biomass burning aerosols and clouds on the $CO_2$
1048       flux in Amazonia, Tellus, Ser. B, 59(3), 338–349.
1049 Oleson, K. W., and Coauthors, 2010: Technical description of version 4.0 of the Community Land Model
1050       (CLM). NCAR Tech. Note NCAR/TN-478+STR, 257 pp.
1051 Oleson, K. W., Lawrence, D. M., Bonan, G. B., Drewniak, B., Huang, M., Koven, C. D., Levis, S., Li,
1052       F., Riley, W. J., Subin, Z. M., Swenson, S. C., Thornton, P. E., Bozbiyik, A., Fisher, R., Heald, C.
1053       L., Kluzek, E., Lamarque, J.-F., Lawrence, P. J., Leung, L. R., Lipscomb, W., Muszala, S., Ricciuto,
1054       D. M., Sacks, W., Sun, Y., Tang, J., & Yang, Z.-L. (2013). Technical description of version 4.5 of
1055       the Community Land Model (CLM), NCAR Tech. Note NCAR/TN-503+STR. National Center for
1056       Atmospheric Research, Boulder, Colorado, 420 pp.
1057 O'Sullivan, M., A. Rap, C. L. Reddington, D. V. Spracklen, M. Gloor, W. Buermann, Small global
1058       effect on terrestrial net primary production due to increased fossil fuel aerosol emissions
1059       from East Asia since the turn of the century, Geophys Res Lett. 2016 Aug 16; 43(15): 8060–
1060       8067. doi: 10.1002/2016GL068965, 2016.
1061 Rap, A., Spracklen, D. V., Mercado, L., Reddington, C. L., Haywood, J. M., Ellis, R. J., Phillips, O. L.,
1062       Artaxo, P., Bonal, D., Restrepo Coupe, N., and Butt, N.: Fires increase amazon forest productivity
1063       through increases in diffuse radiation, Geophys. Res. Lett., 42, 4654–4662
1064       doi:10.1002/2015GL063719, 2015.
1065 Rap, A, Scott, C, Reddington, C, Mercado, L, Ellis, R, Garraway, S, Evans, M, Beerling, D, MacKenzie,
1066       A. R., Hewitt, C. N. and Spracklen, D. V.: Enhanced global primary production by biogenic aerosol
1067       via diffuse radiation fertilisation, Nature Geoscience, vol. 11, pp. 640-644,
1068       https://doi.org/10.1038/s41561-018-0208-3, 2018.
1069 Randles, C. A., Kinne, S., Myhre, G., Schulz, M., Stier, P., Fischer, J., Doppler, L., Highwood, E., Ryder,
1070       C., Harris, B., Huttunen, J., Ma, Y., Pinker, R. T., Mayer, B., Neubauer, D., Hitzenberger, R.,
1071       Oreopoulos, L., Lee, D., Pitari, G., Di Genova, G., Quaas, J., Rose, F. G., Kato, S., Rumbold, S. T.,
1072       Vardavas, I., Hatzianastassiou, N., Matsoukas, C., Yu, H., Zhang, F., Zhang, H., and Lu, P.:
1073       Intercomparison of shortwave radiative transfer schemes in global aerosol modeling: results from the

AeroCom Radiative Transfer Experiment, Atmos. Chem. Phys., 13, 2347–2379, https://doi.org/10.5194/acp-13-2347-2013, 2013.

Randles, C. A., da Silva, A. M., Buchard, V., Colarco, P. R., Darmenov, A., Govindaraju, R., Smirnov, A., Holben, B., Ferrare, R., Hair, J., Shinozuka, Y., and Flynn, C.J.: The MERRA-2 Aerosol Reanalysis, 1980 Onward. Part I: System Description and Data Assimilation Evaluation. J. Clim., 30 (17) (2017), pp. 6823-6850, http://journals.ametsoc.org/doi/10.1175/JCLI-D-16-0613.1, 2017.

Rienecker, M. M., M. J. Suarez, R. Gelaro, R. Todling, J. Bacmeister, E. Liu, M. G. Bosilovich, S. D. Schubert, L. Takacs, G.-K. Kim, S. Bloom, J. Chen, D. Collins, A. Conaty, A. da Silva, W. Gu, J. Joiner, R. D. Koster, R. Lucchesi, A. Molod, T. Owens, S. Pawson, P. Pegion, C. R. Redder, R. Reichle, F. R. Robertson, A. G. Ruddick, M. Sienkiewicz, J. Woollen, MERRA - NASA's Modern-Era Retrospective Analysis for Research and Applications. J. Climate, 24, 3624–3648, 2011.

Roderick, M. L., G. D. Farquhar, S. L. Berry, and I. R. Noble (2001), On the direct effect of clouds and atmospheric particles on the productivity and structure of vegetation, Oecologia, 129(1), 21–30.

Saatchi S, Asefi-Najafabady S, Malhi Y, Arag~ao LEOC, Anderson LO, Myneni RB, Nemani R (2013) Persistent effects of a severe drought on Amazonian forest canopy. Proceedings of the National Academy of Sciences of the United States of America, 110, 565–570.

Schmidt, G. A., et al. (2014), Configura-tion and assessment of the GISS Mod-elE2 contributions to the CMIP5 archive, J. Adv. Model. Earth Syst., 6, 141–184, doi:10.1002/2013MS000265.

Schmidt, G. A., Kelley, M., Nazarenko, L., Ruedy, R., Russell, G. L., Aleinov, I., Bauer, M., Bauer, S. E., Bhat, M. K., Bleck, R., Canuto, V., Chen, Y.-H., Cheng, Y., Clune, T. L., Del Genio, A., de Fainchtein, R., Faluvegi, G., Hansen, J. E., Healy, R. J., Kiang, N. Y., Koch, D., Lacis, A. A., LeGrande, A. N., Lerner, J., Lo, K. K., Matthews, E. E., Menon, S., Miller, R. L., Oinas, V., Oloso, A. O., Perlwitz, J. P., Puma, M. J., Putman, W. M., Rind, D., Romanou, A., Sato, M., Shindell, D. T., Sun, S., Syed, R. A., Tausnev, N., Tsigaridis, K., Unger, N., Voulgarakis, A., Yao, M.-S., Zhang, J. (2014). Configuration and assessment of the GISS ModelE2 contributions to the CMIP5 archive. Journal of Advances in Modeling Earth Systems, 6(1), 141– 184. https://doi.org/10.1002/2013ms000265.

Shilling, J. E., M. S. Pekour, E. C. Fortner, P. Artaxo, S. de Sá, J. M. Hubbe, K. M. Longo, L. A. T. Machado, S. T. Martin, S. R. Springston, J. Tomlinson and J. Wang (2018). "Aircraft Observations of Aerosol in the Manaus Urban Plume and Surrounding Tropical Forest during GoAmazon 2014/15." Atmos. Chem. Phys. Discuss. 2018: 1-37.

Sporre, M. K., Blichner, S. M., Karset, I. H. H., Makkonen, R., and Berntsen, T. K.: BVOC–aerosol–climate feedbacks investigated using NorESM, Atmos. Chem. Phys., 19, 4763–4782, https://doi.org/10.5194/acp-19-4763-2019, 2019.

Strada, S. and Unger, N.: Potential sensitivity of photosynthesis and isoprene emission to direct radiative effects of atmospheric aerosol pollution, Atmos. Chem. Phys., 16, 4213–4234, https://doi.org/10.5194/acp-16-4213-2016, 2016.

Thornton, P. E., & Zimmermann, N. E. (2007). An improved canopy integration scheme for a land surface model with prognostic canopy structure. Journal Of Climate, 20, 3902-3923. doi:10.1175/JCLI4222.1.

Unger, N., Yue, X., and Harper, K. L.: Aerosol climate change effects on land ecosystem services, Faraday Discuss., 200, 121–142, https://doi.org/10.1039/c7fd00033b, 2017.

University of Oklahoma. "Dry season increase in photosynthesis in Amazon rain forest." ScienceDaily. ScienceDaily, 22 October 2019. <www.sciencedaily.com/releases/2019/10/191022092804.htm>

Wang, X., Wu, J., Chen, M., Xu, X., Wang, Z., Wang, B., Wang, C., Piao, S., Lin, W., & Miao, G. (2018). Field evidences for the positive effects of aerosols on tree growth. *Global Change Biology*, **24**, 4983– 4992. https://doi.org/10.1111/gcb.14339.

Wild, O., X. Zhu, and M. Prather, Fast-J: Accurate simulation of in- and below-cloud photolysis in tropospheric chemical models, J. Atmos. Chem. 37, 245-282, 2000.

1124    Xi, X., and I. N. Sokolik, 2012: Impact of Asian dust aerosol and surface albedo on photosynthetically
1125        active radiation and surface radiative balance in dryland ecosystems. Advances in Meteorology, 2012,
1126        Article ID 276207, doi: 10.1155/2012/276207.
1127    Yan, X., W. Z. Shi, W. J. Zhao, et al., 2014: Impact of aerosols and atmospheric particles on plant leaf
1128        proteins. Atmos. Environ., 88, 115–122, doi: https://doi.org/10.1016/j.atmosenv.2014.01.044.
1129    Zhou, Yanlian; Xiaocui Wu; Weimin Ju; Leiming Zhang; Zhi Chen; Wei He; Yibo Liu; Yang Shen,
1130        Modeling the Effects of Global and Diffuse Radiation on Terrestrial Gross Primary Productivity in
1131        China Based on a Two-Leaf Light Use Efficiency Model, *Remote Sens. 12*(20),
1132        3355; https://doi.org/10.3390/rs12203355, 2020.